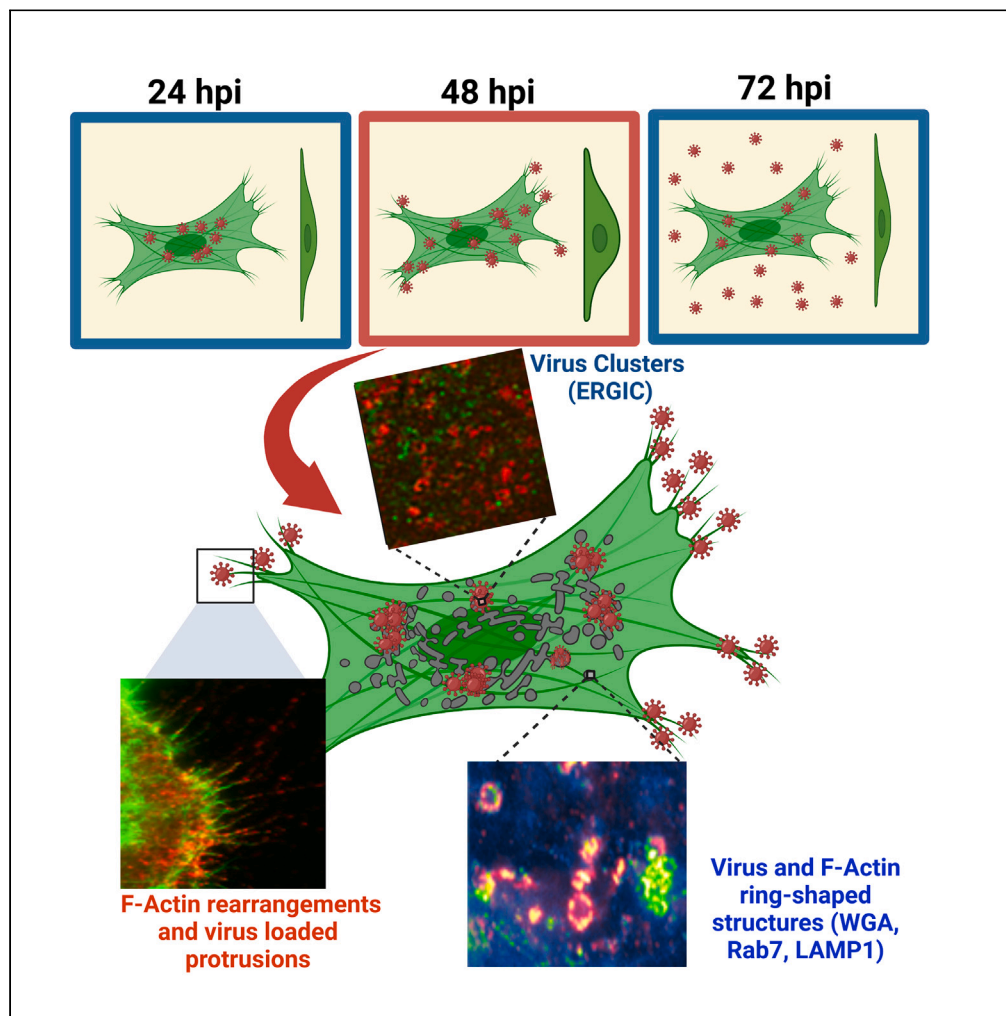


## Article

## F-actin nanostructures rearrangements and regulation are essential for SARS-CoV-2 particle production in host pulmonary cells



Jitendriya Swain,  
Peggy Merida,  
Karla Rubio, ...,  
Stefan Günther,  
Guillermo Barreto,  
Delphine Muriaux

delphine.muriaux@irim.cnrs.fr

**Highlights**

F-actin undergoes strong rearrangement and protrusions during SARS-CoV-2 infection

Filopodia-like nanostructures are induced by infection and loaded with viruses

F-actin ring-like structures surrounded intracellular virus-containing vesicles

PKN inhibition lowers virus particle production and restores F-actin nanostructures

Swain et al., iScience 26,  
107384  
August 18, 2023 © 2023 The  
Author(s).  
[https://doi.org/10.1016/  
j.isci.2023.107384](https://doi.org/10.1016/j.isci.2023.107384)

## Article

## F-actin nanostructures rearrangements and regulation are essential for SARS-CoV-2 particle production in host pulmonary cells

Jitendriya Swain,<sup>1</sup> Peggy Merida,<sup>1</sup> Karla Rubio,<sup>2,3</sup> David Bracquemond,<sup>1</sup> Aymeric Neyret,<sup>4</sup> Israel Aguilar-Ordoñez,<sup>5</sup> Stefan Günther,<sup>6</sup> Guillermo Barreto,<sup>2,3</sup> and Delphine Muriaux<sup>1,4,7,\*</sup>

## SUMMARY

**Our study focused on deciphering the role of F-actin and related regulatory factors during SARS-CoV-2 particle production and transmission in human pulmonary cells. Quantitative high-resolution microscopies revealed that the late phases of SARS-CoV-2 infection induce a strong rearrangement of F-actin nanostructures dependent on the viral M, E, and N structural proteins. Intracellular vesicles containing viral components are labeled with Rab7 and Lamp1 and are surrounded by F-actin ring-shaped structures, suggesting their role in viral trafficking toward the cell membrane for virus release. Furthermore, filopodia-like nanostructures were loaded with viruses, potentially facilitating their egress and transmission between lung cells. Gene expression analysis revealed the involvement of alpha-actinins under the regulation of the protein kinase N (PKN). The use of a PKN inhibitor efficiently reduces virus particle production, restoring endoplasmic reticulum and F-actin cellular shape. Our results highlight an important role of F-actin rearrangements during the productive phases of SARS-CoV-2 particles.**

## INTRODUCTION

Severe acute respiratory syndrome coronavirus 2 (SARS-CoV-2) is a major worldwide public health burden as the main cause of the ongoing COVID-19 pandemic, with over 300 million confirmed cases in 190 countries and more than 6 million deaths to date.<sup>1</sup> SARS-CoV-2 mainly infects human pulmonary cells, destroying the target cells and causing severe respiratory diseases with excessive inflammation that can induce respiratory failure, multi-organ failure, and death.<sup>2</sup> SARS-CoV-2 is an enveloped virus with a positive-sense, single-stranded RNA genome and belongs to the Betacoronavirus family.<sup>3–5</sup> After SARS-CoV-2 infects target cells, intracellular viral replication takes place consisting of a series of complex processes (e.g., viral RNA translation, particle packaging, assembly, and release) that are tightly orchestrated to one another and often mutually exclusive (as well described by Bracquemond et al.<sup>6</sup>). Viral translation often takes place first to create a stock of viral proteins that will serve in assembling the newly made viral particles. The SARS-CoV-2 transcriptome consists of a long unspliced genomic RNA and 9 sub-genomic RNAs generated by alternative splicing. After viral RNA translation, once the structural nucleocapsid protein N is produced in the cytosol of infected cells, SARS-CoV-2 assembly continues with the interactions of the N proteins with the unspliced genomic RNA.<sup>7</sup> These interactions lead to a ribonucleoprotein (RNP) complex that will assemble at the membrane of the endoplasmic reticulum (ER), ER-Golgi intermediate compartment (ERGIC) with the structural transmembrane (M), envelop (E), and spike (S) proteins.<sup>8–10</sup> M is the most abundant and central proteins in the assembly of a particle, and E the protein responsible for budding, after recognition of the RNP with M, E, and S at the ERGIC. Indeed, the cellular expression of these 4 structural proteins is solely able to form virus-like particles.<sup>11</sup> The resulting viral particles, ranging from 90 to 200 nm as recently described,<sup>8,9,12,13</sup> will bud from the ER/ERGIC and egress through the secretory endo-lysosomal pathway.<sup>6,14</sup>

A number of studies over the years have shown that most enveloped viruses hijack the actin cytoskeletal network, underneath the budding membrane, to fulfill their own replication cycle, which motivated us to perform a detailed study on the role of the actin cytoskeleton during SARS-CoV-2 infection in human host pulmonary cells,<sup>14–18</sup> especially on SARS-CoV-2 traffic, assembly, and egress during the late phases

<sup>1</sup>Institute of Research in Infectiology of Montpellier (IRIM), CNRS, University of Montpellier, UMR9004 CNRS, Montpellier, France

<sup>2</sup>Université de Lorraine, CNRS, Laboratoire IMoPA, UMR 7365, 54000 Nancy, France

<sup>3</sup>International Laboratory EPIGEN, Consejo de Ciencia y Tecnología del Estado de Puebla (CONCYTEP), Instituto de Ciencias, Ecocampus, Benemérita Universidad Autónoma de Puebla (BUAP), Puebla 72570, Mexico

<sup>4</sup>CEMIPAI, CNRS, University of Montpellier, UAR3725 CNRS, Montpellier, France

<sup>5</sup>Instituto Nacional de Medicina Genómica (INMEGEN), Mexico City, Mexico

<sup>6</sup>ECCPS Bioinformatics and Deep Sequencing, Max-Planck-Institute for Heart and Lung Research, 61231 Bad Nauheim, Germany

<sup>7</sup>Lead contact

\*Correspondence: [delphine.muriaux@irim.cnrs.fr](mailto:delphine.muriaux@irim.cnrs.fr)

<https://doi.org/10.1016/j.isci.2023.107384>



of the replication cycle. It is well known that the formations of different F-actin nanostructures under the plasma membrane can be a carrier for virus entry or for transfer from one cell to another.<sup>10,14,19,21</sup> It has also been demonstrated that the Rho family of GTPases, which includes the main RhoA, Rac1, and Cdc42 proteins, regulates F-actin dynamics and is important for viral replication.<sup>16,17,20</sup> Thus, targeting F-actin rearrangements has been proposed as a potential therapeutic strategy for inhibiting virus replication and preventing the spread of viral infection. Although the mechanisms of trafficking implicated in SARS-CoV-2 infection have been explored mostly in simian Vero cell lines,<sup>14,22,23</sup> little is known about the participation of F-actin nanostructures during SARS-CoV-2 replication in human pulmonary cells, especially for the late phases, i.e., during particle production. Here, we used confocal and super-resolution 2D and 3D simulated-emission-depletion (STED) microscopy<sup>24</sup> to study the kinetics of M cluster formation during SARS-CoV-2 particle assembly and release, as well as the effects of SARS-CoV-2 infection on intracellular rearrangements of F-actin nanostructures and thus on the morphology of infected human pulmonary cells. The human alveolar pulmonary A549-hACE2 cells were used in this study, as a well-established experimental model for SARS-CoV-2 research in lung cells due to their high susceptibility to SARS-CoV-2 infection, due to the stable overexpression of the human angiotensin-converting enzyme (hACE2), the receptor protein for the viral S protein.<sup>25</sup> Upon infection of these cells by SARS-CoV-2, we have shown that the kinetics of M cluster formation during SARS-CoV-2 particle assembly and release correlate with the polymerization of intracellular F-actin, different structural regulation of F-actin (ring-shaped and filament structures), and consequently morphological changes of the ER and of the infected A549-hACE2 cells. We have shown that the reorganization of F-actin nanostructures is associated with viral M ring-like structures which are vesicles loaded with viruses and carrying the host cell markers Rab7, ERGIC53, and Lamp1 indicating the involvement of the late lyso-endosomes pathway for viral particle assembly and egress in human pulmonary cells. Furthermore, we found that F-actin-related host cell factors alpha-actinins under the regulation of protein kinase N (PKN) are involved as PKN inhibitors significantly reduces viral particle production, restoring ER and F-actin structures inside the infected cells.

## RESULTS

### Polymerization of F-actin nanostructures and cell morphology changes correlate with viral M cluster formation during SARS-CoV-2 particle assembly

To investigate the kinetics of SARS-CoV-2 assembly, we monitored the formations of viral M clusters at different time points after SARS-CoV-2 infection (6–77 h post-infection, pi) using immunofluorescence confocal microscopy with an anti-CoV-2 membrane protein ( $\alpha$ M) antibody (Figures 1A, 1B, S1A, and S2). Human pulmonary A549-hACE2 cells were found to be highly susceptible to SARS-CoV-2 infection (Figures S1 and S2). The size quantification of intracellular M clusters per cell at different time points pi (Figure 1C, left; Figure S1A) showed an increase of intracellular M cluster size from a mean of  $0.6 \mu\text{m}^2$  (interquartile range, IQR  $-0.1 - 3 \mu\text{m}^2$ ) at 24 h pi to a median of  $1.46 \mu\text{m}^2$  (IQR =  $0.4 - 15 \mu\text{m}^2$ ) at 48 h pi. However, the size of intracellular M clusters per cell significantly decreased after 48 h pi to  $0.77 \mu\text{m}^2$  (IQR =  $0.1 - 9 \mu\text{m}^2$ ) at 54 h pi,  $0.72 \mu\text{m}^2$  (IQR =  $0.1 - 8 \mu\text{m}^2$ ) at 72 h pi, and  $0.64 \mu\text{m}^2$  (IQR =  $0.1 - 7 \mu\text{m}^2$ ) at 77 h pi. The maximal area occupied by intracellular M clusters per cell was  $15 \mu\text{m}^2$  at 48 h pi, while it ranged between 3 and  $9 \mu\text{m}^2$  at the other time points analyzed. The quantification of the total intensity of viral M clusters per cell (Figure 1C, right) also showed a significant peak at 48 h pi (mean =  $8.06 \times 10^7$ ) compared to other time points analyzed. Supporting these results, RNA sequencing (RNA-seq)-based expression analysis in SARS-CoV-2-infected A549-hACE2 cells showed a significant increase of all viral transcripts from 24 h pi to 48 h pi (Figure S1C), suggesting an increase of unsliced viral genomic RNA during SARS-CoV-2 assembly. The intracellular increase of the viral structural proteins N, M, and S from 24 h pi to 72 h pi was also detected (Figure S1C), as well as a peak of viral particle release in the cell culture medium at 72 h pi (Figures 1D and S1D). Our results support that during the kinetics of SARS-CoV-2 infection of human pulmonary cells, intracellular SARS-CoV-2 assembly peaks at 48 h pi, while the release of SARS-CoV-2 particles peaks at 72 h pi.

We also monitored the effect of SARS-CoV-2 infection on the actin cytoskeleton of A549-hACE2 cells by confocal microscopy at different time points pi after labeling F-actin with a phalloidin stain (Figures 1E and S2). We observed changes in the distribution of F-actin in A549-hACE2 cells at different time points of SARS-CoV-2 pi. For example, F-actin stress fibers were visible in non-infected control cells and disappeared 24 h pi, while other F-actin structures, such as elongated filopodia-like protrusions, appeared 24 h pi. Further, quantification of F-actin intensity using z stack projection images (Figure 1F) revealed a significant increase of F-actin intensity from 999 a.u. at 0 h pi to 1,572 a.u. at 24 h pi and 1,857 a.u. at 48 h pi, while F-actin intensity decreased to 1,184 a.u. at 72 h pi. Interestingly, we did not detect significant

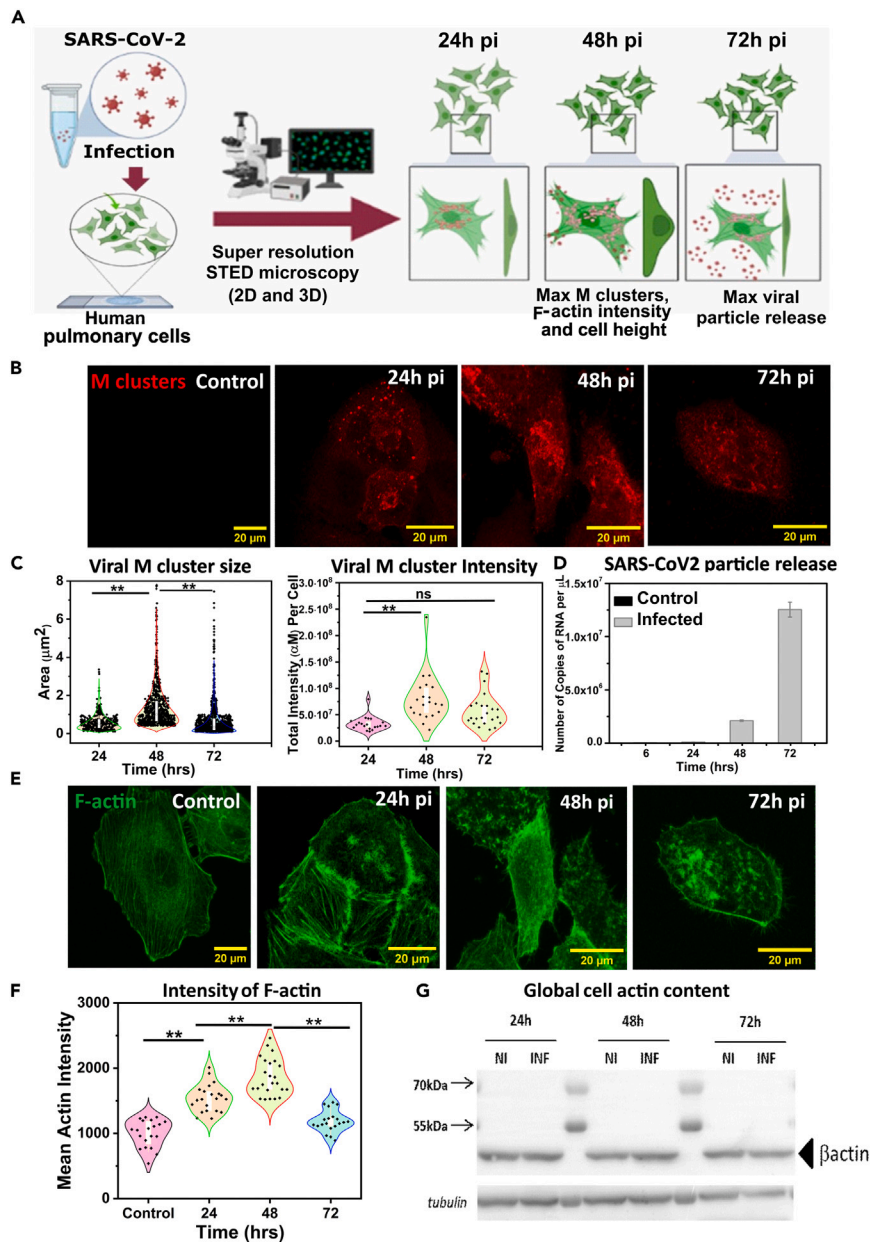


**Figure 1. Increase in cell F-actin content correlated with viral M clusters upon SARS-CoV-2 infection in lung cells**

(A) Schematic representation of experimental details used for confocal images of viral clusters and F-actin at different time (0h–72h) post-infection in the host pulmonary A549hACE2 cell line (referred as lung cells).

(B) Confocal images of viral M clusters (in red color) in lung cells at different time point post-infection with an anti-M antibody.

(C) Plot showing viral M clusters size ( $n = 331, 687$  and  $<700$  M clusters for 24h pi, 48h pi and 72h pi, respectively) and viral M clusters intensity at different time point post-infection ( $n = 21, 22,$  and  $22$  for 24h pi, 48h pi and 72h pi, respectively).

(D) Plot showing number of copies of viral RNA/ $\mu\text{L}$  by qRT-PCR in the supernatant of infected cells at different time point post-infection.

(E) Confocal images showing changes in F-actin (in green color) intensity per cell at different time point post-infection. Phalloidin-A4888 is used for F-actin labeling.

(F) Plot showing mean F-actin intensity per cell with or without infection at different time point post-infection ( $n = 21, 22, 24$  and  $20$  cells for control, 24h pi, 48h pi, and 72h pi, respectively).

(G) Representative immunoblot showing global cell actin content of non-infected and infected cells at different time point post-infection. One-way analysis of variance (ANOVA) and Mann-Whitney test was used for group comparisons. ns,  $p > 0.05$ ,  $*p \leq 0.05$ ,  $**p \leq 0.01$ ,  $***p \leq 0.001$ , and  $****p \leq 0.0001$ . Each point is mean SD of  $n = 3$  independent experiments. Scale bar is  $20 \mu\text{m}$  for all images.

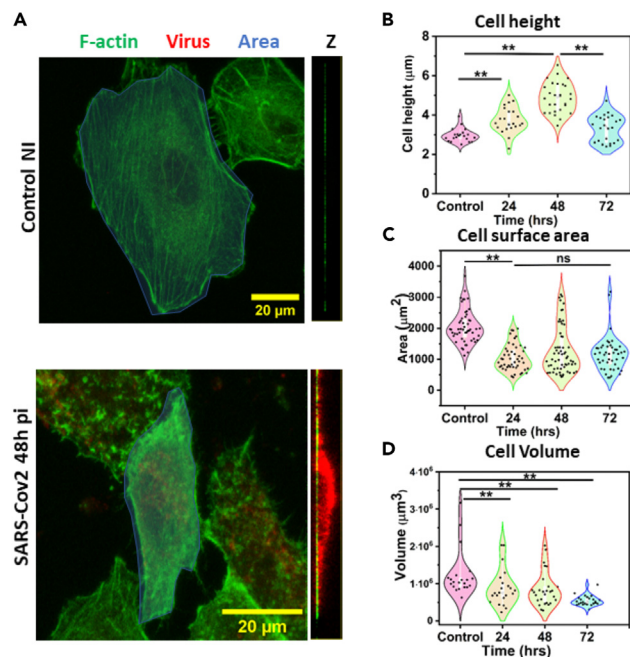


**Figure 2. F-actin reorganization and cell morphological changes upon SARS-CoV-2 infection in lung cells**

(A) Confocal images of not infected (control NI) and CoV-2-infected A549-hACE2 cells (48h pi) with viral M (in red) and F-actin labeling (in green).  
 (B) Plot showing changes in cell height at different time points (n = 22 cells for control, 24h pi, 48h pi, and 72h pi).  
 (C) Plot showing changes in surface area of the cells at different time points (n = 52, 48, 61 and 45 cells for control, 24h pi, 48h pi, and 72h pi, respectively).  
 (D) Plot showing cell volume of the cells at different time points (n = 21, 22, 28 and 24 cells for control, 24h pi, 48h pi, and 72h pi, respectively). One-way analysis of variance (ANOVA) and Mann-Whitney test was used for group comparisons. ns,  $p > 0.05$ , \* $p \leq 0.05$ , \*\* $p \leq 0.01$ , \*\*\* $p \leq 0.001$ , and \*\*\*\* $p \leq 0.0001$ . Each point is mean SD of n = 3 independent experiments. Scale bar is 20  $\mu\text{m}$  for all images.

changes in the total actin content of the cell by western blot (WB) analysis of proteins extracts (Figure 1G). Our results indicate that SARS-CoV-2 infection induced extensive polymerization of intracellular actin fibers without significantly affecting total actin levels. Further analysis of the morphological changes that we observed in A549-hACE2 cells upon SARS-CoV-2 infection was quantified in fixed cells (Figures 2A and 2B) and revealed significant increase in cell height from 2.96  $\mu\text{m}$  (IQR = 2.2–3.9  $\mu\text{m}$ ) at 0 h pi to 3.75  $\mu\text{m}$  (IQR = 2.2–4.72  $\mu\text{m}$ ) at 24 h pi and 4.89  $\mu\text{m}$  (IQR = 3.4–6  $\mu\text{m}$ ) at 48 h pi, while cell height decreased to 3.29  $\mu\text{m}$  (IQR = 2.4–4.8  $\mu\text{m}$ ) at 72 h pi. In contrast to cell height, cell surface and cell volume showed opposite effects upon SARS-CoV-2 infection with decreasing values after 24 h pi (Figures 2C and 2D), suggesting a contraction of the A549-hACE2 cells at this time point. Summarizing, our results indicate that the kinetics of M cluster formation during SARS-CoV-2 particle assembly and release correlate with rearrangements of intracellular actin fibers and morphological changes of SARS-CoV-2-infected human A549-hACE2 lung cells.

### Viral assembly regulates F-actin nanostructure formation (ring-shaped and filopodia-like protrusions) during the late phases of SARS-CoV-2 infection

We focused our analysis on the time point of maximum M cluster formation during SARS-CoV-2 assembly, which was observed at 48 h pi. To improve the resolution of our imaging, we used super-resolution 2D STED microscopy in both non-infected and SARS-CoV-2-infected A549-hACE2 cells (Figures 3A and S3). This increased the resolution to below 70 nm, which is 10 times better than what was possible with confocal microscopy. To quantify F-actin rearrangements, we have analyzed the orientation angle of actin fibers from STED images (as described by Blanchoin et al.,<sup>18</sup>). Our results showed that in non-infected cells, actin stress fibers were parallel, while they were not visible in SARS-CoV-2-infected cells at 48 h pi (Figure 3A). The color map of F-actin orientation and data for the distribution of orientation angle suggested a significant rearrangement of the F-actin network with protrusion of filaments at the cell plasma membrane

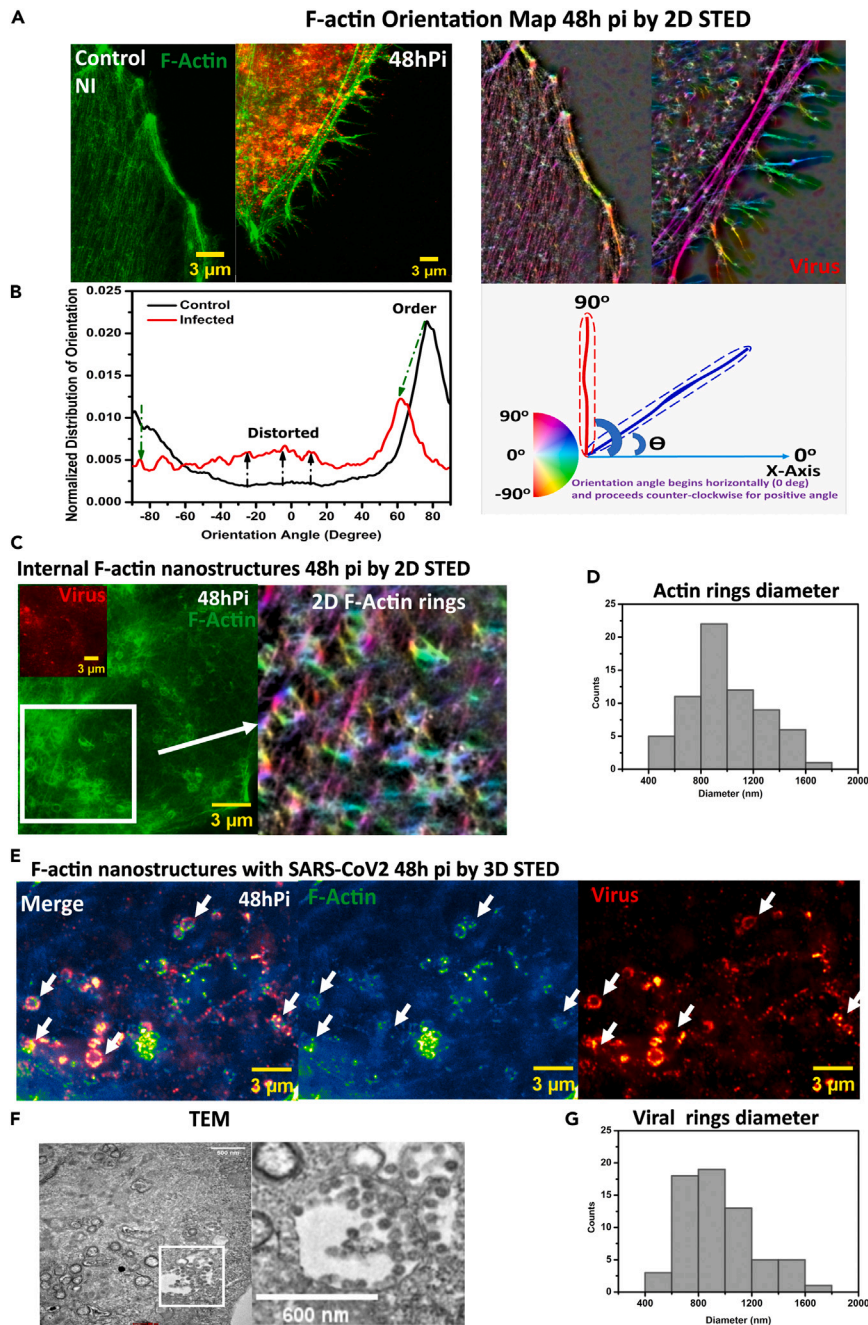


**Figure 3. F-actin nanostructures reorganization and intracellular actin ring-shaped formation during the late steps of SARS-CoV-2 infection in lung cells**

STED 2D and 3D images of showing the changes in F-actin and viral M clusters of SARS-CoV-2 in infected lung cells (48 hpi). Viral M (in red), F-actin (in green).

(A) STED 2D images and color representation of orientation angles of F-actin network in lung cells without (left panel – control NI) or with (right panel - 48hpi) infection.

(B) Plot showing the distribution of F-actin orientation angles, without (in black) or with (in red) infection.

(C) STED 2D images of actin rings with pseudo color representation of the rings.

(D) Histogram showing the distribution of F-Actin ring diameters (n = 68).

(E) STED 3D images of intracellular viral M rings and F-actin labeling in infected lung cells.

(F) Transmission electron microscopy (TEM) images of intracellular structures filled with budding viruses in SARS-CoV-2-infected lung cells.

**Figure 3. Continued**

(G) Histogram showing the distribution of intracellular viral ring diameters (n = 64). One-way analysis of variance (ANOVA) and Mann-Whitney test was used for group comparisons. ns,  $p > 0.05$ , \* $p \leq 0.05$ , \*\* $p \leq 0.01$ , \*\*\* $p \leq 0.001$ , and \*\*\*\* $p \leq 0.0001$ . Each point is mean SD of n = 3 independent experiments. For TEM images, scale bars are 500 and 600 nm for the zoomed image, as indicated. Scale bar is 3  $\mu\text{m}$  for all STED images.

(Figures 3A and 3B). The major possible orientation angle of F-actin fibers in non-infected cells was significantly lower (around 90 and -90°) than that in SARS-CoV-2-infected cells at 48 h pi (Figure 3B). We also detected an increase in the random orientation angle after infection, probably due to F-actin rearrangement, distortion, or reorganization. To investigate the potential formation of intracellular self-organizing F-actin structures in SARS-CoV-2-infected A549-hACE2 cells, we monitored the organization of the F-actin cytoskeleton at 48 h pi using super-resolution 2D microscopy and detected in the infected cells F-actin structures resembling intracellular “actin rings” (Figure 3C). The diameter of the observed “actin rings” ranged between 0.5 and 2.5  $\mu\text{m}$  with a mean of 1.03  $\mu\text{m}$  and a standard deviation (SD) of 0.35  $\mu\text{m}$  (Figure 3D). However, detection of viral M clusters around intracellular “actin rings” by 2D STED microscopy was limited by signal saturation in Z direction. To bypass these limitations, super-resolution 3D STED microscopy with 185 nm slice in Z direction was implemented (Figure 3E) and surprisingly revealed that viral M clusters formed similar “ring-like” structures in close proximity to the “actin rings”. Transmission electron microscopy (TEM) slices of the infected cells also show vesicular structures, of 0.6–1  $\mu\text{m}$  size, full of viruses with particle budding events at the cell membranes (Figures 3F and S4). By STED 3D, the diameter of the “viral rings” ranged between 0.5 and 2  $\mu\text{m}$  with a mean of 0.95  $\mu\text{m}$  and an SD of 0.27  $\mu\text{m}$  (Figure 3G). By superposing both F-actin and virus ring STED images, it appears that M-labeled intracellular organelles (“viral rings”) are surrounded by F-actin nanostructures (“actin rings”) (Figure 3E).

Further, to investigate the other F-actin structures during virus particle egress, we have used super-resolution 2D STED microscopy with quantitative analysis (Figures 4A–4C). We observed that the number of F-actin protrusions significantly increased in SARS-CoV-2-infected cells 48 h pi ranging from 2 per 10  $\mu\text{m}$  of infected cell plasma membrane (IQR = 1–3) in non-infected lung cells to 10 per 10  $\mu\text{m}$  of infected cell plasma membrane (IQR = 6–18) (Figure 4B). We also detected a significant increase in the maximum length of F-actin protrusions structures from 2 to 4  $\mu\text{m}$  in non-infected cells to 10–12  $\mu\text{m}$  in SARS-CoV-2-infected cells 48 h pi (Figure 4C). Interestingly, we observed these structures loaded with viruses. A quantitative analysis of the viral M clusters and individual particles using 2D/3D STED images revealed three different populations of viral M clusters in three different cellular regions that are able to regulate different F-actin nano-structures for transfer and egress: intracellular ring-like structure (see Figure 3E), particle release sites at the edge of the cell plasma membrane (Figure S5A, zone 1), and viral particles at the filopodia-like protrusions of infected cells (Figure S5A, zone 2). The size of viral particles ranged in zone 2 from 70 nm to 350 nm with a mean of 209 nm and an SD of 87 nm (Figure S5A) and in zone 1 from 150 nm to 1,000 nm (Mean = 478 nm; SD = 216 nm; Figure S5A). These quantitative analyses suggested that viral particles could release in packages at the cell membrane and then viral particles could “migrate” on or inside filopodia-like structures. Strikingly, in some infected cells at close proximity, we also observed an inter-connection between cells via filopodia-like structures enriched with F-actin and loaded with viruses, suggesting that virus-containing filopodia like structures could be one of the possible mechanisms for cell-to-cell SARS-CoV-2 infection spread in lung cells (Figures S5A and S3). Our results allow the hypothesis of a spatial and functional interplay between different F-actin nanostructures and viral M cluster formation during assembly of SARS-CoV-2 particles, suggesting a stabilization of the viral assembly platforms by F-actin or the need for F-actin for the transport of virus-loaded vesicles toward the cell plasma membrane and outside of the cell. Further, we observed similar F-actin rearrangements and protrusions in SARS-CoV-2-infected VeroE6 cells, another cell line, at 48 h pi (Figure S5C). Quantification of filopodia-like structures loaded with viruses shows means of 1.57 per 10  $\mu\text{m}$  of cell plasma membrane (IQR = 1–3) in non-infected cells to 10.67 per 10  $\mu\text{m}$  in infected cells (IQR = 5–17). These results suggest that the virus is able to induced F-actin protrusions independently of the cell type.

We further investigated the effect of the assembly of SARS-CoV-2 structural proteins on F-actin rearrangement and protrusions. We performed a series of cell transfections to examine independently cells expressing membrane (M), nucleocapsid (N), envelope (E), and spike (S) proteins with confocal or STED microscopy (Figures 4D and 4E). As M is known to be the major driver of particle assembly in coronaviruses, we transfected combinations of structural proteins with M. We used triple combinations such as M + E + N, M + N + S, M + E + S, and M + N + E + S (Figure 4D). Surprisingly, only the all-structural protein combination

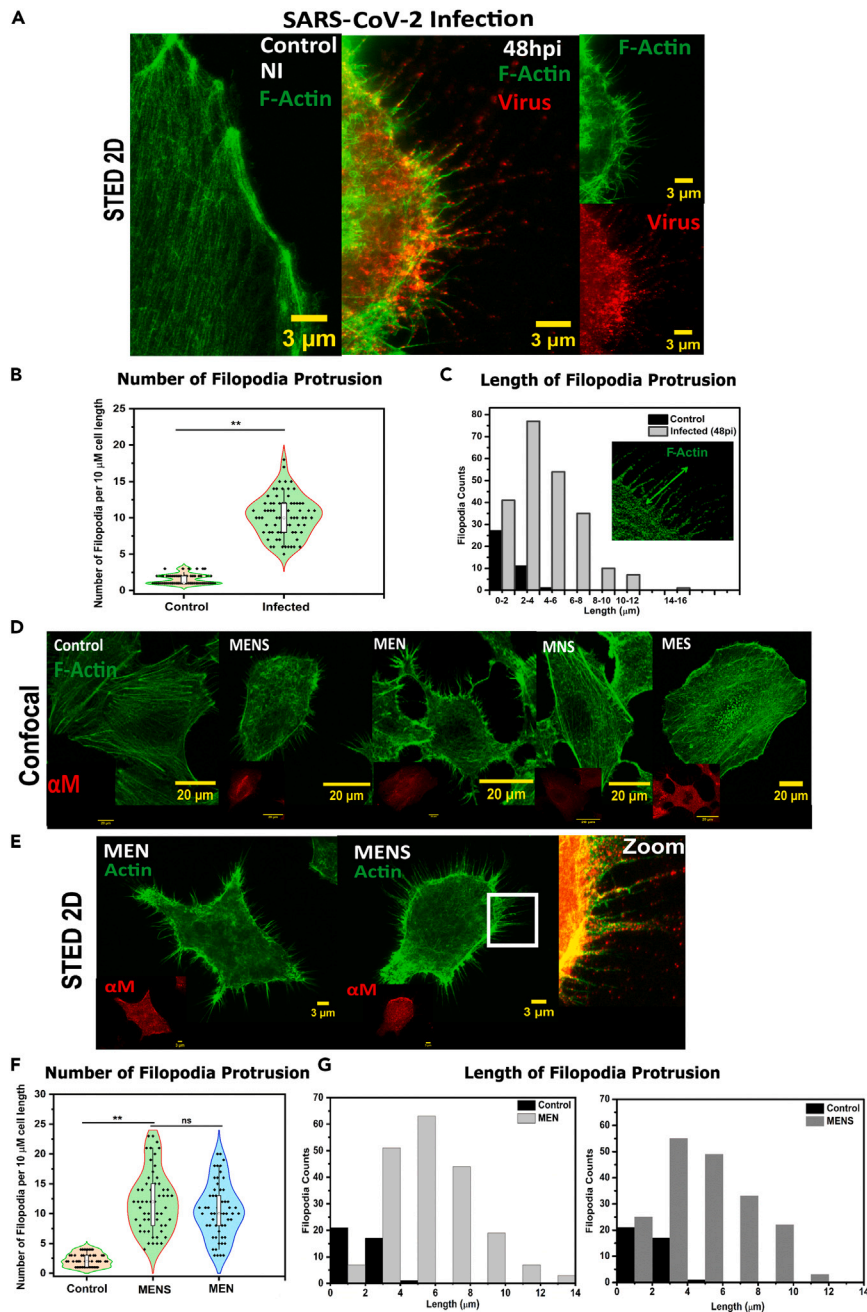


**Figure 4. Reorganization of F-actin nanostructures into virus-loaded filopodia-like protrusions at the cell surface of SARS-CoV-2-infected or transfected lung cells**

STED 2D images and quantitative data analysis of changes in F-actin nanostructures in SARS-CoV-2-infected A549-hACE2 cells (48h pi). Viral M (in red) and F-actin (in green) are shown.

(A) Merge STED 2D images of control (NI) and 48h pi lung cells.

(B) Plot showing the distribution of the number of filopodia per 10  $\mu\text{m}$  lengths for each cell infected or non-infected control ( $n = 15$ ).

(C) Plot showing the distribution of the length of individual filopodia in control and infected lung cells ( $n = 15$ ).

(D) Confocal images showing F-actin labeling of lung cells with or without transfection with different combination of SARS-CoV-2 structural proteins, as indicated MENS, MNE, MEN, MNS, and MES.

(E) STED 2D images of MENS and MES transfected lung cells (48h ptr) with viral M clusters (in red) and F-actin labeling (in green). Zoomed images showing VLP on the filopodia-like protrusions.

**Figure 4. Continued**

(F) Plot showing distribution of the number of filopodia-like protrusions per 10  $\mu\text{m}$  length for each cell, 48h post-transfection for MNES and MNE and control conditions (n = 15).

(G) Plot showing the distribution of the length of individual filopodia-like protrusions in transfected cells for the MENS, MEN and control (n = 15). One-way analysis of variance (ANOVA) and Mann-Whitney test was used for group comparisons. ns,  $p > 0.05$ ,  $*p \leq 0.05$ ,  $**p \leq 0.01$ ,  $***p \leq 0.001$ , and  $****p \leq 0.0001$ . Each point is mean SD of n = 3 independent experiments. Scale bar is 20  $\mu\text{m}$  for confocal images and 3  $\mu\text{m}$  for STED images.

M + E + N + S and the triple combination M + E + N were able to significantly rearrange F-actin structures (Figure 4E). In transfected cells expressing MENS or MEN, F-actin formed long filamentous filopodia-like structures (Figures 4D and 4E) as it is the case with the WT virus-infected cells (Figures 4A–4C). These two combinations were also analyzed with STED 2D imaging technique for further quantitative analysis on actin rearrangement and filopodia-like structure formation (Figures 4F and 4G). In STED 2D imaging, we observed a distribution of 4–20 numbers of F-actin protrusions per 10  $\mu\text{m}$  of cell length in both combinations of transfection as compare to 1 to 4 numbers in case of control cell (Figure 4F). In case of transfected cell (MENS and MEN 48 h post-transfection), the F-actin protrusions length distributed from 2 to 15  $\mu\text{m}$  with maximum number of F-actin protrusions at 2–8  $\mu\text{m}$  length (Figure 4G). Thus, the cell expression of the combination of the structural SARS-CoV-2 proteins M, N, and E is critical for actin cytoskeleton rearrangements. These are also the conditions for leading to VLP (virus-like particles) assembly and egress (as shown by Gourdelier et al.,<sup>11</sup>; Figure 4E zoom image showing M-labeled VLP on filopodia-like structures).

**F-actin ring-shaped nanostructures are associated with virus-loaded vesicles**

Production of SARS-CoV-2 particles in lung cells is a multistep process that occurs in different compartments of the infected cells that culminate in the assembly of viral components inside the cell, followed by the egress of infectious virus particles at the cell membrane. To go further in the characterization of these intracellular SARS-CoV-2 M ring-shaped structures, most probably containing new viral particles in formation, we performed quantitative high-resolution Airy scan 3-color confocal microscopy on SARS-CoV-2-infected lung cells at 48 h pi during the productive step of viral particles (Figures 5 and S6) with several vesicular markers. All indicated that these are vesicles, since M is a viral transmembrane protein, and they are labeled with the membranous WGA (wheat germ agglutinin) marker (Figures 5A and S6A). We observed a strong colocalization between the WGA marker (membrane), the ring-shaped M clusters, and F-actin, as well as with the viral nucleocapsid protein N and S (Figure S7) strongly suggesting that virus-loaded vesicles surrounded by F-actin are containing assembling particles. We furthermore tried different vesicular markers, such as ERGIC (viral particle assembly location), Rab7 (late endosomes), Lamp1 (endo-lysosomes), and EEA1 (early endosomes), and analyzed their colocalization with M-labeled vesicles (Figure 5). We discovered that these vesicles do not contain any early endosomes marker and partially contain ERGIC-53 marker (with 53% of colocalization with M) (Figures 5C and S6). However, M-labeled vesicles were strongly colocalized with Rab7 (75%)-harboring vesicles (Figures 5B and 5C) and partially with Lamp1 (55%) lysosomes. Furthermore, the size of the Rab7(+) and Lamp1(+) vesicles containing M were significantly enhanced in size upon infection: Rab7(+) vesicles' mean diameter ranged from 509 nm for non-infected cells to 780 nm for infected cells, Lamp1(+) vesicle's mean diameter ranged from 730 nm for non-infected cells to 941 nm for infected cells (Figures 5D and S6C). The Rab7-harboring vesicles are well colocalized (75%) with both viral M and F-actin ring-shaped structures (Figure 5E). These observations showed that viral M ring-shaped structures were highly positive with Rab7 and F-actin but only to a lesser extent for Lamp1. These results suggest that SARS-CoV-2 productive vesicles hijack the late endosomal pathway with F-actin, probably for trafficking and egress in lung cells.

**SARS-CoV-2 infection enhances expression of actin cytoskeleton regulating genes**

Our results suggest that F-actin rearrangements during viral particle assembly are important for viral replication during SARS-CoV-2 infection progression. To gain further insights, we performed an RNA-seq-based transcriptome analysis in non-infected and SARS-CoV-2-infected A549-hACE2 cells at 48 h pi (Figures 6A and S8A). We detected increased levels after infection in 9.91% of the transcripts mapped to the human genome (4,376 transcripts with  $FC \geq 2$ ), whereas the levels of 7.10% of the transcripts mapped to the human genome were reduced (3,136 transcripts with  $FC \leq 0.3$ ). Gene set enrichment analysis (GSEA) based on Reactome<sup>26</sup> from the top 9.91% of the genes with increased levels 48 h pi (4,376 transcripts; Figure 6B) revealed significant enrichment of genes related to RhoGTPases activate PKNs ( $p = 0.368$ ) as the top item of the ranked list. In addition, graphical representation of the enrichment profile showed a high enrichment score (ES) of 0.559 for RhoGTPases activate PKNs (Figure 6C). The immunofluorescence of PKN

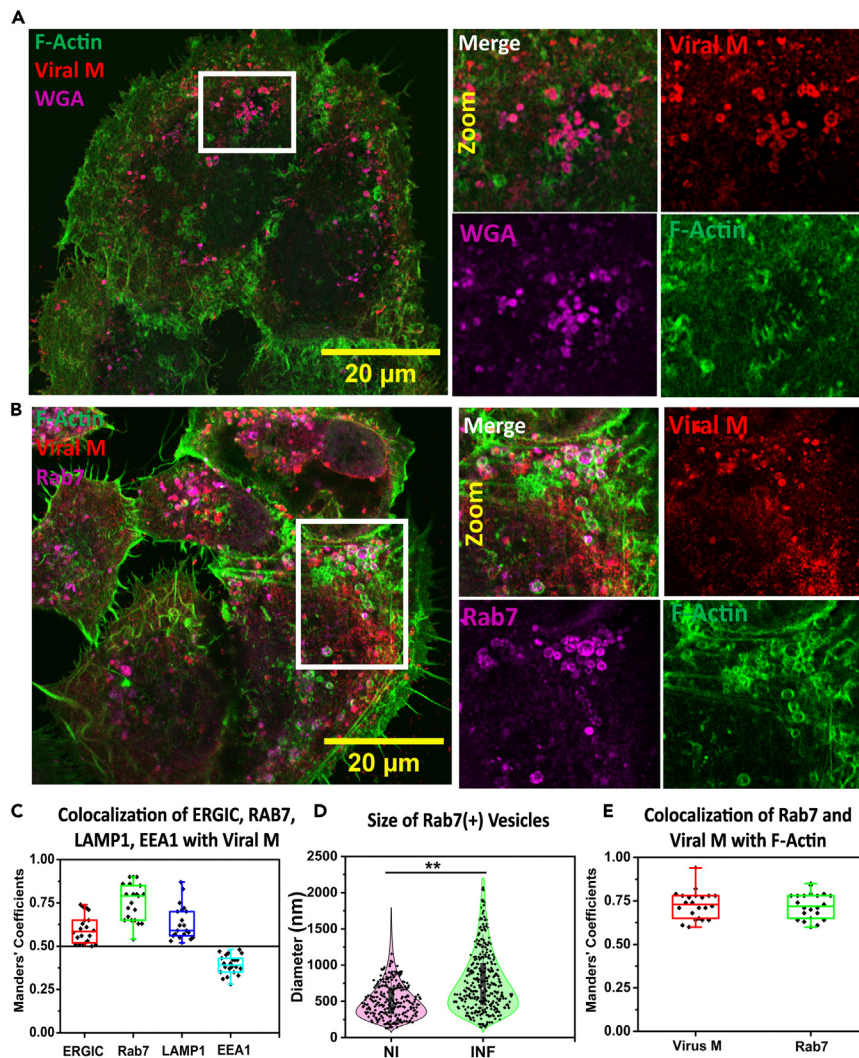


**Figure 5. Intracellular F-actin and viral M ring-shaped structures are Rab7, Lamp1 and ERGIC marker-positive vesicles**

High-resolution Airy Scan images of F-actin, cellular organelles and viral M clusters of SARS-CoV-2-infected lung cells. (A) Airy Scan confocal images with zoom area of A549-hACE2-infected cells 48 hpi showing intracellular viral M rings (in red), F-actin rings (in green) and WGA-labeled membrane rings (in magenta). (B) Airy Scan confocal images with zoomed area of A549-hACE2-infected cells showing viral M rings (in red), F-actin rings (in green) and Rab7 harboring rings (in magenta). (C) Plot showing Mander's colocalization coefficient between ERGIC, Rab7, LAMP1, EEA1 with Viral M (n = 24). (D) Plot showing diameters of Rab7-positive vesicles without (NI) versus with infection (INF) (n = 250). (E) Plot showing Mander's colocalization coefficient between Rab7 and viral M with F-actin (n = 25). One-way analysis of variance (ANOVA) and Mann-Whitney test was used for group comparisons. ns,  $p > 0.05$ , \* $p \leq 0.05$ , \*\* $p \leq 0.01$ , \*\*\* $p \leq 0.001$ , and \*\*\*\* $p \leq 0.0001$ . Each point is mean SD of n = 3 independent experiments. Scale bar is 20  $\mu$ m.

protein is well correlated with earlier results (Figure 6D). Since RhoGTPases are best known for their roles in regulating cytoskeletal rearrangements, we monitored the transcript levels of various proteins related to the cytoskeleton and detected increased transcript levels of proteins that are known to be regulated by RhoGTPases, thereby being Alpha-actinin superfamily, and in particular Alpha-Actinins 2 and 3 (ACTN2, ACTN3), the ones with the most prominent increase (Figure 6E). Type II myosins are also reported (MHY7 and MHY6), suggesting together with ACTN2 and ACTN3 a possible contractile activity of the infected cells,<sup>27</sup> as previously suggested by our cell morphology analysis (Figure 2) or being only of structural nature. In addition, 2D STED microscopy images and actin orientation analysis (Figure 3A) revealed the formation of large actin fibers at the cell plasma membrane of infected cells. Furthermore, immunoblots

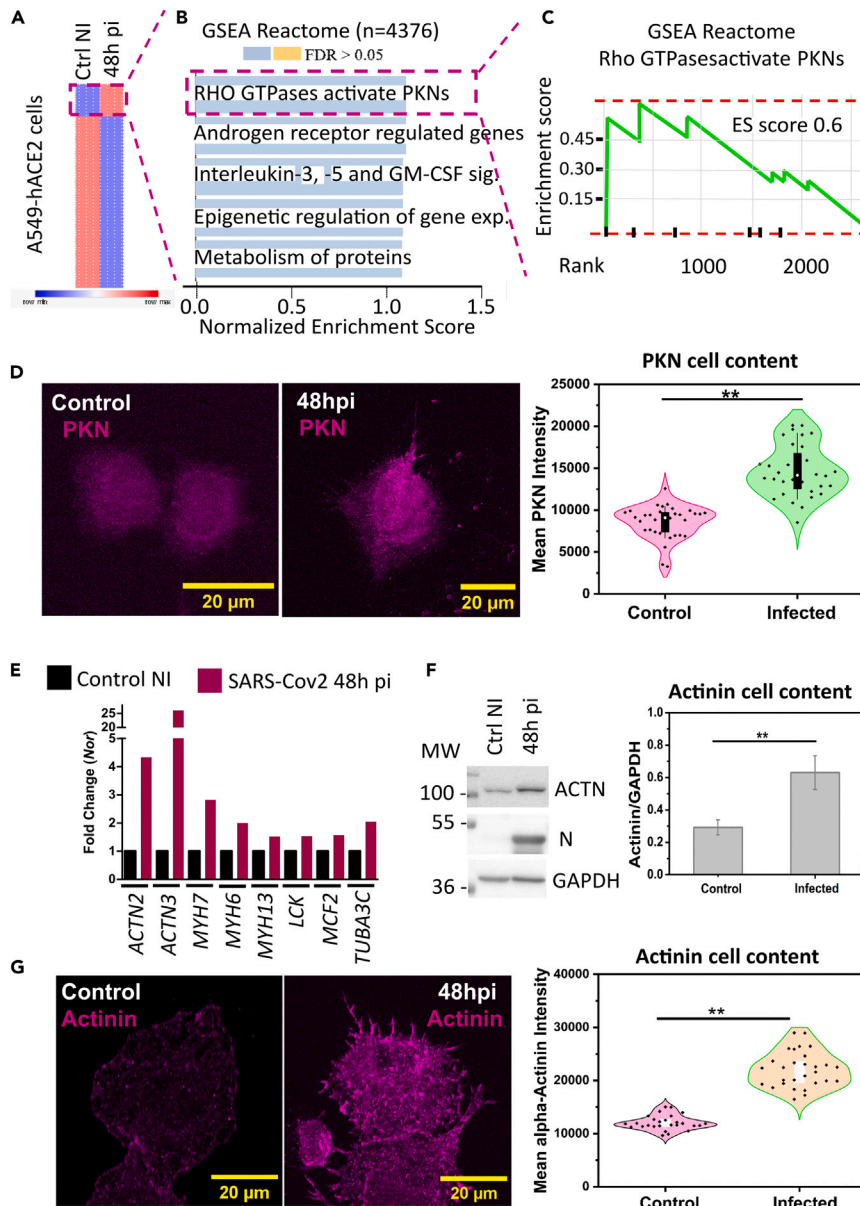


**Figure 6. Cellular gene expression analysis of SARS-CoV-2-infected lung cells using RNAseq reveals an upregulation of Protein Kinase N and alpha-Actinins**

(A) Heatmap showing RNA-seq-based expression analysis of differentially expressed transcripts in non-infected (Control NI) and A549hACE2 lung cells infected with SARS-CoV-2 (48h pi). n = 44141 differentially expressed transcripts; 2 individual cell replicates per condition.

(B) Top. Reactome-based Gene Set Enrichment Analysis (GSEA) of candidates with FC ≥ 2 (n = 4376 upregulated transcripts) using WebGestalt (WEB-based Gene Set Analysis Toolkit, 2019). Bottom. Panther-based Gene Set Enrichment Analysis (GSEA) of candidates with FC ≤ 0.3 (n = 3136 downregulated transcripts) using WebGestalt (WEB-based Gene Set Analysis Toolkit, 2019). FDR: False Discovery Rate.

(C) Reactome-based Gene Set Enrichment Analysis (GSEA) for RhoGTPases pathway of candidates with FC ≥ 2.

(D) Immunofluorescence images and PKN mean fluorescence intensity analyzed for control and infected cells (48h pi) (n = 30).

(E) Histogram plots representing the basal transcription activity (48h pi normalized to Control NI) of components of the Rho-GTPase pathway that are differentially expressed in Control (NI) and SARS-CoV-2-infected lung cells.

(F) Representative immunoblot and quantitative plots showing alpha-actinin expression both in control and infected cells (48h pi).

**Figure 6. Continued**

(G) Confocal images and plots for alpha-actinin mean fluorescence intensity for control and infected cells (48h pi) (number of cells analyzed  $n = 28$ ). One-way analysis of variance (ANOVA) and Mann-Whitney test was used for group comparisons. ns,  $p > 0.05$ , \* $p \leq 0.05$ , \*\* $p \leq 0.01$ , \*\*\* $p \leq 0.001$ , and \*\*\*\* $p \leq 0.0001$ . Each point is mean SD of  $n = 3$  independent experiments. Scale bar is 20  $\mu\text{m}$  for all images.

revealed a 2-fold increase of alpha-Actinins (ACTN) in SARS-CoV-2-infected cell extract, 48 h pi, as compared to non-infected cell extracts (Figure 6F). Finally, quantitative immunofluorescence confocal microscopy revealed that the mean fluorescence intensity of alpha-Actinins was enhanced by 2-fold, as well, with SARS-CoV-2 infection as compared to non-infected pulmonary cells (Figure 6G).

**Actin regulator proteins inhibitors reduced SARS-CoV-2 replication in human pulmonary cells**

Following the line of ideas from our previous results (Figures 2, 3, and 5), we have investigated the effect of the 3 inhibitors of Rho/SFR, Rac1, and PKN on SARS-CoV-2 replication since they regulate actin fiber formation and alpha-actinin regulation for PKN. The data show that Rho/SFR and PKN inhibitors reduce SARS-CoV-2 replication in human pulmonary cells over time and in a dose-dependent manner, with IC<sub>50</sub> (inhibitory concentration 50) values of 1.35  $\mu\text{M}$  and 0.65  $\mu\text{M}$ , respectively (Figures 7A, S9A, and S9C). The Rac1 inhibitor EHT1864 at 50  $\mu\text{M}$  also inhibits SARS-CoV-2 replication without causing toxicity as revealed by RTqPCR (reverse transcription-polymerase chain reaction) gene E (Figure S9D). The lethal dose 50 (LD<sub>50</sub>) for the Rho/SFR inhibitor was 7.02  $\mu\text{M}$  and 37.7  $\mu\text{M}$  for the PKN inhibitor, with a selectivity index greater than 10, indicating that these are potent antiviral inhibitors for the development of therapeutic strategies against SARS-CoV-2. PKN inhibitor was also able to decrease by approximately 4-fold the level of viral particle release 48 h pi with continuous treatment of the cells (Figure 7B). Moreover, confocal immunofluorescence images of human pulmonary A549-hACE2 cells infected with SARS-CoV-2 in the presence of 0.5  $\mu\text{M}$  PKN inhibitor showed a restoration of cell morphology like height, volume, and area and of the F-actin structural pattern as compared to infected cells (Figures 7C, S10, and S11). Also, we were not able to observe any filopodia-like protrusion in the presence of 0.5  $\mu\text{M}$  PKN inhibitor (or Remdesivir, as a control drug). Strikingly, PKN inhibitor treatment of SARS-CoV-2-infected pulmonary cells reduced the size of intracellular viral M clusters (Figure 7D). We have used Remdesivir (IC<sub>50</sub> equal to 1  $\mu\text{M}$ ) as positive control for viral inhibition for these experiments since it is a well-known antiviral drug that targets the virus replication complex,<sup>28</sup> also showing F-actin restoration and M cluster reduction in infected cells (Figure S12). For further investigations of M cluster localization, we investigated the colocalization of M protein and a marker (GRP78) of the ER. We observed a 75% colocalization from the Manders coefficient analysis between viral M clusters and ER-GRP78 marker in the infected cells (Figure 7E). In addition, we observed a significant enhancement of ER-GRP78 level (observed from mean ER intensity), which is spread all over the cell, associated with viral M proteins in infected cells as compared to non-infected cells (Figures 7C, 7F, and S11), as reported by Kösele et al and Sabirli et al.<sup>29,30</sup> Interestingly, the PKN inhibitor was able to block M clusters in the ER, as shown in Figure 7C, as well as partially restore the ER distortion, by means of the intensity and localization of ER-GRP78 in PKN-treated infected cells, as in non-infected cells (Figures 7F and S11). The above results suggested that inhibiting PKN or related protein kinase family that regulates F-actin leads to a significant decrease in virus replication as well as a decrease in viral particle release, and virus is now blocked at the ER level (Figure 7).

**DISCUSSION**

SARS-CoV-2 is a recently discovered virus. Despite the fact that it is in the spotlight of the scientific community worldwide for being the main cause of the COVID-19 pandemic, the role of the cytoskeleton, in particular of actin fibers, during SARS-CoV-2 replication in lung cells has remained vague. Here, we implemented quantitative confocal and super-resolution 2D and 3D STED microscopies, as well as gene profiling using transcriptomics, to evaluate F-actin rearrangement and actin-associated proteins during the late phases of SARS-CoV-2 infection in human alveolar pulmonary cells, the primary target of SARS-CoV-2. Here, we report that intracellular SARS-CoV-2 M clusters responsible for particle assembly and F-actin both strongly increase at 48 h pi, accompanied with concerted cell morphology deformations followed by a strong viral particle release at 72 h pi (Figures 1 and 2). The RNA-seq-based analysis of viral transcripts at 48 h pi (Figure S1) correlated with the increase of SARS-CoV-2 infection signing the late phases in our study. The apparent discrepancies between our SARS-CoV-2 transcriptome and the recently published SARS-CoV-2 transcriptome<sup>31</sup> could be explained by differences in the experimental design, such as the implementation of different cell lines (Calu-3, Caco-2, and Vero cells versus A549-hACE2) and higher viral

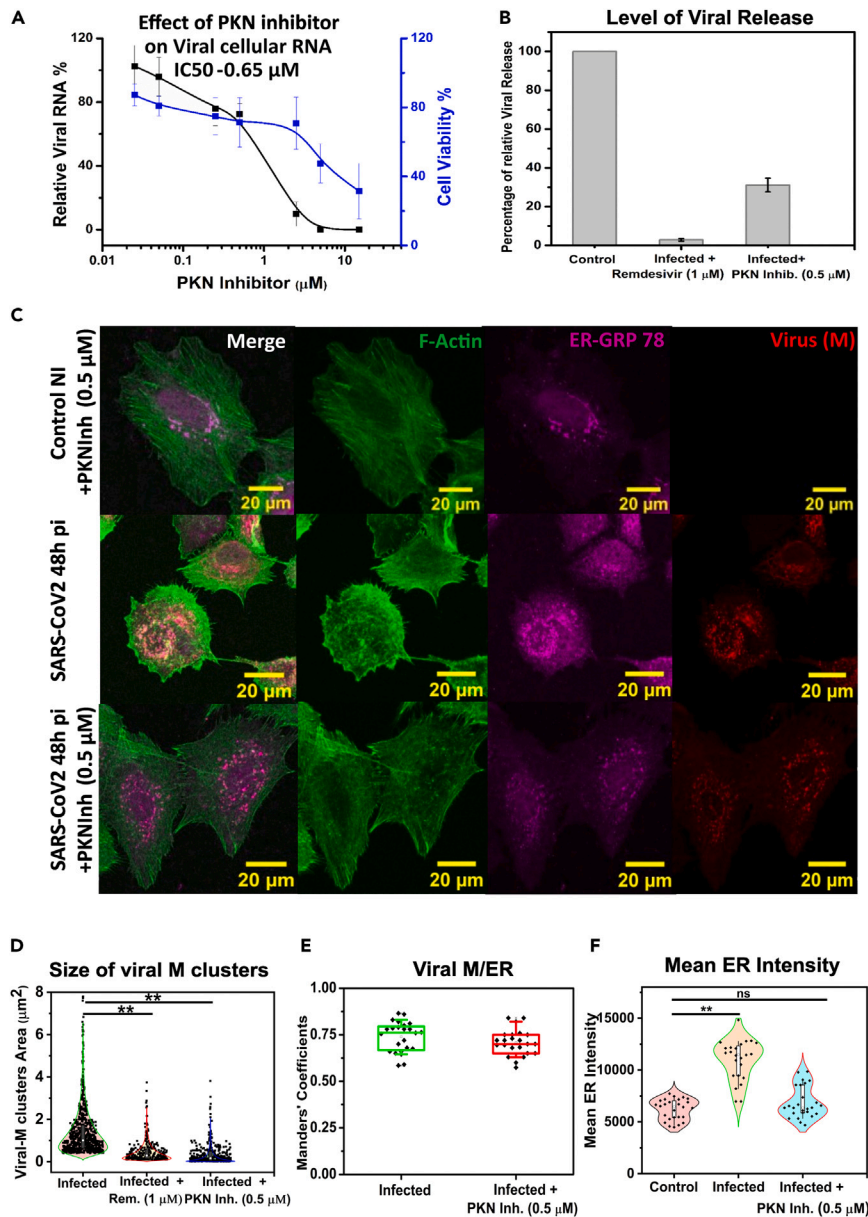


**Figure 7. Reduction of SARS-CoV-2 replication in lung cells upon PKN inhibitor treatment correlated with cellular F-actin and ER-shape restoration**

(A) Plot showing dose dependent effect of PKN inhibitor on SARS-CoV-2 replication in lung cells using qRT-PCR (gene E) and cell viability.

(B) Plot showing number of copies of RNA/ $\mu$ L in the supernatant of infected cells 48h pi with or without treatment of Remdesivir (1  $\mu$ M) or PKN Inhibitor (0.5  $\mu$ M).

(C) Confocal images of A549-hACE2 lung cells without (control NI), with infection (SARS-CoV-2 48h pi) and with PKN inhibitor (0.5  $\mu$ M); viral M (in red), F-Actin (in green), and ER-GRP78 (in magenta) labeling are shown.

(D) Plot showing changes in viral M cluster size in infected cells with or without Remdesivir (Rem) (1  $\mu$ M) or PKN Inhibitor (0.5  $\mu$ M) (n = 500, 259 and 347) in infected cells.

(E) Plot showing Mander's colocalization coefficient between Viral M and ER-GRP78 for infected and infected + PKN inhibitor treated lung cells (n = 23–24 cells).

(F) Plot showing mean ER-GRP78 fluorescence intensity without infection (control) or with infection in the absence or presence of PKN inhibitor (0.5  $\mu$ M) as indicated (n = 26, 24, 26 cells respectively). One-way analysis of variance (ANOVA) and Mann-Whitney test was used for group comparisons. ns, p > 0.05, \*p  $\leq$  0.05, \*\*p  $\leq$  0.01, \*\*\*p  $\leq$  0.001, and \*\*\*\*p  $\leq$  0.0001. Each point is mean SD of n = 3 independent experiments. Scale bar is 20  $\mu$ m for all images.

titters (MOI 1 and 0.1 versus 0.01), among others. Because our human pulmonary A549-hACE2 cell line was very susceptible to SARS-CoV-2 infection (maybe due to high level of hACE2 receptor on the surface), we used lower viral titers during our RNA-seq experiment (MOI 0.01).

More importantly, the observed kinetics of M cluster formation during SARS-CoV-2 particle assembly and release correlated with polymerization of cytoskeletal F-actin nanostructures, regulation of different nanostructures, and morphological changes of A549-hACE2 cells infected with SARS-CoV-2. Our results agree with previous reports demonstrating that actin rearrangements are involved during the replication of various viruses targeting the respiratory tract, including the respiratory syncytial virus (RSV) and influenza A virus.<sup>32–35</sup> Further, the strong cytopathic effect observed after SARS-CoV-2 infection in lung cells could be related to the dramatic changes in F-actin nanostructures and cell morphology. The significance of the cellular morphological changes caused by SARS-CoV-2 infection has revealed a contraction-like effect on the infected cells (Figure 2). This could account for lung tissue destruction leading to fibrosis in the pulmonary tissue, which is consistent with the lung damage observed in the case of COVID-19.<sup>36,37</sup> However, the expression of caspases as apoptosis markers was reduced in SARS-CoV-2-infected cells at 48 h pi, supporting the viability of the cells analyzed here (Figure S7). It is well known that actin polymerization has a role in the replication of influenza viruses.<sup>38</sup> For the respiratory syncytial virus, actin was not completely proven to be involved in assembly; rather, actin was playing a role in virus spread-driven filopodia induction through Arp2/3 complexes.<sup>33</sup> Remarkably, we found that the SARS-CoV-2 infection induces F-actin ring-shaped nanostructures surrounding ring-shaped viral M clusters (Figure 3), revealing the formation of large intracellular virus-containing compartments (VCCs). These vacuoles are enriched in endo-lysosomal markers (Figure 5) in which SARS-CoV-2 particle assembly takes place (Figure 3F), if we refer to the size of these VCC.<sup>39–41</sup> A recent investigation of SARS-CoV-2-infected cells utilizing correlative confocal fluorescence and cryo-electron tomography revealed the presence of virus "exit tunnels" connecting virion-rich intracellular vacuoles to the extracellular space on other cell lines (simian VeroE6 and SH-SY5Y cells).<sup>42</sup> The authors suggested that SARS-CoV-2 could possibly egress through these tunnels by a mechanism of exocytosis from these large intracellular vacuoles. However, they have pointed out that these mechanisms are very cell type specific and would require more investigation.

Our results agree with earlier discoveries, showing that large intracellular structures at the ER/ERGIC contain SARS-CoV-2 structural proteins (M, N, E, and S proteins) together with the viral genomic RNA and drive the assembly of new viral particles.<sup>8,9,14</sup> In our study, the viral M and F-actin ring-shaped nanostructures were significantly labeled with Rab7 and, to a lesser extent, Lamp1, indicating vesicular traffic of SARS-CoV-2-harboring vesicles through the late endo-lysosomal pathway (Figure 5) that may also be regulated by Rac1 in human A549hACE2 lung cells (Figure S9D). This is in good agreement with a previous study on another Betacoronavirus, the murine hepatitis virus (MHV) infection in HeLa and Vero cell lines, also showing the involvement of the lysosomal pathway for coronavirus egress<sup>43</sup> and with a more recent study showing the accumulation of S in the Golgi and ERGIC with lysosomes (Lamp1+) during SARS-CoV-2 late infection stages in another cell type, i.e., Vero cells.<sup>14</sup> In our study, using high-resolution STED 3D and Airy scan analysis, we further characterized the sizes of these virus-containing vacuoles at the cell periphery and found approximately 600 nm to 1  $\mu\text{m}$  (Figure 3) compatible with transport vesicles loaded with viruses. These VCCs were the F-actin and viral ring-shaped structures identified as WGA (lectin binding glycoproteins/glycolipids) and viral M protein-positive vesicles (Figure 5). On the contrary, viral M clusters, which do not form ring-shaped structures, were only well colocalized with the ER-grp78 and ERGIC53 markers, at 48 h pi, and not with the early endosomal antigen (EEA1) marker (Figures 5 and 7). This suggests an accumulation of viral M-labeled particles in the late endo-lysosomal pathway during the late phases of SARS-CoV-2 replication in human pulmonary cells (48 h pi). Thus, the formation of F-actin ring-shaped nanostructures may play a crucial role during viral particles trafficking through the late endosomal pathway preceding particle release/egress (occurring at 72 h pi in our lung cells).

SARS-CoV-2 infection promotes F-actin protrusions loaded with viruses to neighboring cells, suggesting that these structures are a mechanism for SARS-CoV-2 infection spread from cell to cell. Consistent with these findings, viral cell-to-cell transmission has been reported for other RNA enveloped viruses, such as the human immunodeficiency virus 1 (HIV-1),<sup>44</sup> and recently for SARS-CoV-2.<sup>38</sup> In our study, F-Actin polymerization is observed in filopodia-like structures loaded with viruses suggesting a spread of individual viral particles to uninfected cells (Figure S5A), which seems quite different from the reported TNT (tunneling nanotubes) pathway.<sup>42</sup> Indeed, TEM sections or cryo-tomography electron microscopy or

cryo/FIB/SEM (beam scanning electron microscopy) ultrastructure microscopy has shown the formation of filopodia-like structures on which individual viral particles are attached and responsible for cell-to-cell transmission in SARS-CoV-2-infected different cell types (Simian Vero, Human A549-hACE2, Calu3 lung cells).<sup>45,46</sup> These studies are in good agreement with our 2D STED imaging (Figures 4 and S5A) showing filopodia-like structures loaded with viruses. In addition, we identify that these filopodia-like structures, labeled with actin, are induced by only the expression of 3 structural SARS-CoV-2 M, N, E proteins (Figure 4) which are also able to produce VLPs. Summarizing, all these results support a spatial and functional interplay between F-actin nanostructures and viral M clusters during SARS-CoV-2 particle production, by helping the transport of virions through the endo-lysosomal pathway (Figure 5) to the cell plasma membrane for egress, but also for the transport to neighbor cells (Figure S5A) with filopodia-like protrusions. Recently, similar conclusions were indeed shown in a complex airway epithelia system showing that SARS-CoV-2 infection in ciliated cells was able to induce the growth of microvilli (resembling “filopodia-like” protrusions in lung A549hACE2 cells - Figure 4A - and VeroE6 cells – Figure S5C) during the late phase of infection for the viral particles to egress and to propagate in the lung epithelia.<sup>47</sup>

The polymerization of actin and the reorganization of actin filaments are complex processes regulated by different factors. One of these factors is the PKN, which is a fatty acid-activated serine/threonine kinase, whose catalytic domain exhibits homology with that of the protein kinase C family. It has been reported that the interaction of PKN with alpha-actinins is promoted by phosphatidylinositol 4,5-bisphosphate<sup>48,49</sup> suggesting that PKN/alpha-actinin complexes locate at the cell plasma membrane to promote cortical actin fiber rearrangement.<sup>49</sup> Alpha-actinins belong to the spectrin gene superfamily, which represents a diverse group of cytoskeletal proteins. Alpha-actinins are F-actin-crosslinking proteins found in various subcellular localizations both in muscle and non-muscle cells,<sup>50</sup> and they are involved in diverse cellular processes. Besides the involvement of alpha-actinins regulating cortical actin dynamics during HIV-1 entry,<sup>51</sup> the role of alpha-actinins during virus replication has remained largely unknown. Here, we showed that SARS-CoV-2 infection increased levels of ACTN2 and ACTN3 transcripts of ACTN proteins. Furthermore, interfering with alpha-actinins function through PKN inhibitor treatment in SARS-CoV-2-infected cells impaired SARS-CoV-2 replication, reduced viral particle release, blocked in the ER, and restored cell morphology and the F-actin cellular profile (Figures 7 and S11). It supports the idea of using derivatives of PKN inhibitors for the development of new therapeutic approaches against SARS-CoV-2 infection.

Overall, our results reveal that severe F-actin rearrangement occurs upon SARS-CoV-2 infection, generating novel F-actin nanostructures, i.e., ring-shaped and filopodia-like nanostructures loaded with viruses, accompanied by an increase in alpha-actinins and PKN cell content. These F-actin nanostructures are induced and required for the late phases of SARS-CoV-2 replication and for transmission in 2D cultured lung cells, and it would be of interest to further study them in 3D primary pulmonary cells.

### Limitations of the study

The dependence on *in vitro* cell culture methods, which may not fully mimic the complexity of the human respiratory system, is one of the study’s limitations. Furthermore, the study focuses on a narrow collection of actin cell host cofactors, perhaps leaving out other key components. The long-term consequences and clinical significance of the detected F-actin rearrangements have yet to be determined. To address these limitations and give a thorough understanding of role of F-actin in SARS-CoV-2 infection, more research utilizing multiple cellular model systems is required.

### STAR★METHODS

Detailed methods are provided in the online version of this paper and include the following:

- [KEY RESOURCES TABLE](#)
- [RESOURCE AVAILABILITY](#)
  - Lead contact
  - Materials availability
  - Data and code availability
- [METHOD DETAILS](#)
  - Cell culture and infection
  - Transfected cells
  - Immuno-fluorescence confocal, Airy Scan and 2D/3D STED super-resolution microscopy

- Quantitative reverse transcription polymerase chain reaction (qRT-PCR)
- RNA sequencing and data analysis
- RNA-seq based expression analysis of viral transcripts
- Western Blot analysis
- Electron microscopy
- **QUANTIFICATION AND STATISTICAL ANALYSIS**
- Image analysis
- Angle of orientation analysis
- Statistical analysis

## SUPPLEMENTAL INFORMATION

Supplemental information can be found online at <https://doi.org/10.1016/j.isci.2023.107384>.

## ACKNOWLEDGMENTS

We thank CEMIPAI UAR3725 CNRS-University of Montpellier service unit for initial advices on SARS-CoV-2 virus production and titration and for the original TEM sample preparation. The Microscopy STED was done at the Montpellier Imaging Center for Microscopy (MRI). We are very grateful to Marie-Pierre Blanchard for initiation and training on the STED microscope and to Dr Frederic Eghiaian from Abberior for the gift of STED compatible secondary antibodies.

Funding: Delphine Muriaux was funded by the “Centre National de la Recherche Scientifique” (CNRS, France), Montpellier University through a Montpellier University of Excellence (MUSE) and ETINCELL grant support and by the French Agency for Research (ANR COVID19) grant “NucleoCoV-2”. J.Swain was funded by the Mediterranée foundation, Marseille, France and the ETINCELL-UM program. Guillermo Barreto was funded by the “Centre National de la Recherche Scientifique” (CNRS, France), “Délégation Centre-Est” (CNRS-DR6), the “Lorraine Université” (LU, France) through the initiative “Lorraine Université d’Excellence” (LUE) and the dispositive “Future Leader” and the “Deutsche Forschungsgemeinschaft” (DFG, Bonn, Germany) (BA 4036/4-1). Karla Rubio was funded by the “Consejo de Ciencia y Tecnología del Estado de Puebla” (CONCYTEP, Puebla, Mexico) through the initiative International Laboratory EPIGEN.

## AUTHOR CONTRIBUTIONS

D.M. directed the study. P.M. and D.B. performed cell culture, BSL3 infection, viral stock amplification and titer, viral RNA extraction and qRT-PCR, and immunoblots. D.B. and A.N. performed TEM imaging. J.S. performed immunofluorescence sample preparation, confocal, airy scan and STED 2D and 3D Microscopy, and quantitative analysis. K.R. performed RNA extraction and sequencing. K.R., I.A., S.G., and G.B. performed RNA sequencing and analyzed RNA-seq data. J.S., D.M., G.B., and K.R. were involved in manuscript writing. J.S., G.B., and D.M. conceptualized the study, edited the figures, and contributed to editing and reviewing. J.S. and D.M. wrote the original manuscript. D.M. and G.B. raised funding for the study.

## DECLARATION OF INTERESTS

The authors declare no competing interests.

Received: November 30, 2022

Revised: March 24, 2023

Accepted: July 11, 2023

Published: July 17, 2023

## REFERENCES

1. WHO Coronavirus (COVID-19) Dashboard. <https://covid19.who.int/>.
2. Tay, M.Z., Poh, C.M., Rénia, L., MacAry, P.A., and Ng, L.F.P. (2020). The trinity of COVID-19: immunity, inflammation and intervention. *Nat. Rev. Immunol.* 20, 363–374. <https://doi.org/10.1038/s41577-020-0311-8>.
3. Wen, Z., Zhang, Y., Lin, Z., Shi, K., and Jiu, Y. (2020). Cytoskeleton - A crucial key in host cell for coronavirus infection. *J. Mol. Cell Biol.* 12, 968–979. <https://doi.org/10.1093/jmcb/mjaa042>.
4. Liu, Y., Yang, Y., Zhang, C., Huang, F., Wang, F., Yuan, J., Wang, Z., Li, J., Li, J., Feng, C., et al. (2020). Clinical and biochemical indexes from 2019-nCoV infected patients linked to viral loads and lung injury. *Sci. China Life Sci.* 63, 364–374. <https://doi.org/10.1007/s11427-020-1643-8>.
5. Yang, Y., Zhang, L., Geng, H., Deng, Y., Huang, B., Guo, Y., Zhao, Z., and Tan, W. (2013). The structural and accessory proteins M, ORF 4a, ORF 4b, and ORF 5 of Middle East respiratory syndrome

- coronavirus (MERS-CoV) are potent interferon antagonists. *Protein Cell* 4, 951–961. <https://doi.org/10.1007/s13238-013-3096-8>.
6. Bracquemond, D., and Muriaux, D. (2021). Betacoronavirus Assembly: Clues and Perspectives for Elucidating SARS-CoV-2 Particle Formation and Egress. *mBio* 12, e0237121. <https://doi.org/10.1128/mbio.02371-21>.
  7. Cascarina, S.M., and Ross, E.D. (2022). Phase separation by the SARS-CoV-2 nucleocapsid protein: Consensus and open questions. *J. Biol. Chem.* 298, 101677. <https://doi.org/10.1016/j.jbc.2022.101677>.
  8. Liu, C., Mendonça, L., Yang, Y., Gao, Y., Shen, C., Liu, J., Ni, T., Ju, B., Liu, C., Tang, X., et al. (2020). The Architecture of Inactivated SARS-CoV-2 with Postfusion Spikes Revealed by Cryo-EM and Cryo-ET. *Structure* 28, 1218–1224.e4. <https://doi.org/10.1016/j.str.2020.10.001>.
  9. Bar-On, Y.M., Flamholz, A., Phillips, R., and Milo, R. (2020). Sars-cov-2 (Covid-19) by the numbers. *Elife* 9, e57309. <https://doi.org/10.7554/eLife.57309>.
  10. Caldas, L.A., Carneiro, F.A., Higa, L.M., Monteiro, F.L., da Silva, G.P., da Costa, L.J., Durigon, E.L., Tanuri, A., and de Souza, W. (2020). Ultrastructural analysis of SARS-CoV-2 interactions with the host cell via high resolution scanning electron microscopy. *Sci. Rep.* 10, 16099. <https://doi.org/10.1038/s41598-020-73162-5>.
  11. Gourdelier, M., Swain, J., Arone, C., Mouttou, A., Bracquemond, D., Merida, P., Saffarian, S., Lyonnais, S., Favard, C., and Muriaux, D. (2022). Optimized production and fluorescent labeling of SARS-CoV-2 virus-like particles. *Sci. Rep.* 12, 14651. <https://doi.org/10.1038/s41598-022-18681-z>.
  12. Yao, H., Song, Y., Chen, Y., Wu, N., Xu, J., Sun, C., Zhang, J., Weng, T., Zhang, Z., Wu, Z., et al. (2020). Molecular Architecture of the SARS-CoV-2 Virus. *Cell* 183, 730–738.e13. <https://doi.org/10.1016/j.cell.2020.09.018>.
  13. Lyonnais, S., Hénaut, M., Neyret, A., Merida, P., Cazeville, C., Gros, N., Chable-Bessia, C., and Muriaux, D. (2021). Atomic force microscopy analysis of native infectious and inactivated SARS-CoV-2 virions. *Sci. Rep.* 11, 11885. <https://doi.org/10.1038/s41598-021-91371-4>.
  14. Scherer, K.M., Mascheroni, L., Carnell, G.W., Wunderlich, L.C.S., Makarchuk, S., Brockhoff, M., Mela, I., Fernandez-Villegas, A., Barysevich, M., Stewart, H., et al. (2022). SARS-CoV-2 nucleocapsid protein adheres to replication organelles before viral assembly at the Golgi/ERGIC and lysosome-mediated egress. *Sci. Adv.* 8, eab4895. <https://doi.org/10.1126/sciadv.ab4895>.
  15. le Clainche, C., and Carrier, M.F. (2008). Regulation of actin assembly associated with protrusion and adhesion in cell migration. *Physiol. Rev.* 88, 489–513. <https://doi.org/10.1152/physrev.00021.2007>.
  16. Gil, P.I., Albrieu-Llinás, G., Mlewski, E.C., Monetti, M., Fozzatti, L., Cuffini, C., Fernández Romero, J., Kunda, P., and Paglini, M.G. (2017). Pixuna virus modifies host cell cytoskeleton to secure infection. *Sci. Rep.* 7, 5757. <https://doi.org/10.1038/s41598-017-05983-w>.
  17. Zan, J., An, S.T., Mo, K.K., Zhou, J.W., Liu, J., Wang, H.L., Yan, Y., Liao, M., and Zhou, J.Y. (2016). Rabies virus inactivates cofilin to facilitate viral budding and release. *Biochem. Biophys. Res. Commun.* 477, 1045–1050. <https://doi.org/10.1016/j.bbrc.2016.07.030>.
  18. Blanchoin, L., Boujema-Paterski, R., Sykes, C., and Plastino, J. (2014). Actin dynamics, architecture, and mechanics in cell motility. *Physiol. Rev.* 94, 235–263. <https://doi.org/10.1152/physrev.00018.2013>.
  19. Nemethova, M., Auinger, S., and Small, J.V. (2008). Building the actin cytoskeleton: Filopodia contribute to the construction of contractile bundles in the lamella. *J. Cell Biol.* 180, 1233–1244. <https://doi.org/10.1083/jcb.200709134>.
  20. Sun, X., and Whittaker, G.R. (2007). Role of the actin cytoskeleton during influenza virus internalization into polarized epithelial cells. *Cell Microbiol.* 9, 1672–1682. <https://doi.org/10.1111/j.1462-5822.2007.00900.x>.
  21. Fritzsche, M., Li, D., Colin-York, H., Chang, V.T., Moeendarbary, E., Felce, J.H., Sezgin, E., Charras, G., Betzig, E., and Eggeling, C. (2017). Self-organizing actin patterns shape membrane architecture but not cell mechanics. *Nat. Commun.* 8, 14347. <https://doi.org/10.1038/ncomms14347>.
  22. Bouhaddou, M., Memon, D., Meyer, B., White, K.M., Rezelj, V.v., Correa Marrero, M., Polacco, B.J., Melnyk, J.E., Sifert, S., Kaake, R.M., et al. (2020). The Global Phosphorylation Landscape of SARS-CoV-2 Infection. *Cell* 182, 685–712.e19. <https://doi.org/10.1016/j.cell.2020.06.034>.
  23. Cortese, M., Lee, J.Y., Cerikan, B., Neufeldt, C.J., Oorschot, V.M.J., Köhrer, S., Hennies, J., Schieber, N.L., Ronchi, P., Mizzon, G., et al. (2020). Integrative Imaging Reveals SARS-CoV-2-Induced Reshaping of Subcellular Morphologies. *Cell Host Microbe* 28, 853–866.e5. <https://doi.org/10.1016/j.chom.2020.11.003>.
  24. Favard, C., Chojnacki, J., Merida, P., Yandrapalli, N., Mak, J., Eggeling, C., and Muriaux, D. (2019). HIV-1 Gag specifically restricts PI(4,5)P2 and cholesterol mobility in living cells creating a nanodomain platform for virus assembly. *Sci. Adv.* 5, eaaw8651. <https://doi.org/10.1126/sciadv.aaw8651>.
  25. Letko, M., Marzi, A., and Munster, V. (2020). Functional assessment of cell entry and receptor usage for SARS-CoV-2 and other lineage B betacoronaviruses. *Nat. Microbiol.* 5, 562–569. <https://doi.org/10.1038/s41564-020-0688-y>.
  26. Subramanian, A., Tamayo, P., Mootha, V.K., Mukherjee, S., Ebert, B.L., Gillette, M.A., Paulovich, A., Pomeroy, S.L., Golub, T.R., Lander, E.S., and Mesirov, J.P. (2005). Gene set enrichment analysis: A knowledge-based approach for interpreting genome-wide expression profiles. *Proc. Natl. Acad. Sci. USA* 102, 15545–15550. <https://doi.org/10.1073/pnas.0506580102>.
  27. Levayer, R., and Lecuit, T. (2012). Biomechanical regulation of contractility: Spatial control and dynamics. *Trends Cell Biol.* 22, 61–81. <https://doi.org/10.1016/j.tcb.2011.10.001>.
  28. Chable-Bessia, C., Boullé, C., Neyret, A., Swain, J., Hénaut, M., Merida, P., Gros, N., Makinson, A., Lyonnais, S., Chesnais, C., and Muriaux, D. (2022). Low Selectivity Indices of Ivermectin and Macrocyclic Lactones on SARS-CoV-2 Replication In Vitro. *COVID* 2, 60–75. <https://doi.org/10.3390/covid2010005>.
  29. Köseleler, A., Sabirli, R., Gören, T., Türkçüer, I., and Kurt, Ö. (2020). Endoplasmic reticulum stress markers in SARS-COV-2 infection and pneumonia: Case-control study. *Vivo (Brooklyn)* 34. <https://doi.org/10.21873/invivo.11956>.
  30. Sabirli, R., Köseleler, A., Gören, T., Türkçüer, I., and Kurt, Ö. (2021). High GRP78 levels in Covid-19 infection: A case-control study. *Life Sci.* 265, 118781. <https://doi.org/10.1016/j.lfs.2020.118781>.
  31. Kim, D., Kim, S., Park, J., Chang, H.R., Chang, J., Ahn, J., Park, H., Park, J., Son, N., Kang, G., et al. (2021). A high-resolution temporal atlas of the SARS-CoV-2 transcriptome and transcriptome. *Nat. Commun.* 12, 5120. <https://doi.org/10.1038/s41467-021-25361-5>.
  32. Shahriari, S., Gordon, J., and Ghildyal, R. (2016). Host cytoskeleton in respiratory syncytial virus assembly and budding. *Virology* 531, 161. <https://doi.org/10.1016/j.virus.2016.06.018-z>.
  33. Mehedi, M., McCarty, T., Martin, S.E., Le Nouën, C., Buehler, E., Chen, Y.C., Smelkinson, M., Ganesan, S., Fischer, E.R., Brock, L.G., et al. (2016). Actin-Related Protein 2 (ARP2) and Virus-Induced Filopodia Facilitate Human Respiratory Syncytial Virus Spread. *PLoS Pathog.* 12, e1006062. <https://doi.org/10.1371/journal.ppat.1006062>.
  34. Ada, G.L., Perry, B.T., and Edney, M. (1957). Infectivity of influenza virus filaments [2]. *Nature* 180, 1134. <https://doi.org/10.1038/1801134a0>.
  35. Mosley, V.M., and Wyckoff, R.W.G. (1946). Electron micrography of the virus of influenza [2]. *Nature* 157, 263. <https://doi.org/10.1038/157263a0>.
  36. Valdebenito, S., Bessis, S., Annane, D., Lorin de la Grandmaison, G., Cramer-Bordé, E., Prideaux, B., Eugenin, E.A., and Bomsel, M. (2021). COVID-19 Lung Pathogenesis in SARS-CoV-2 Autopsy Cases. *Front. Immunol.* 12, 735922. <https://doi.org/10.3389/fimmu.2021.735922>.
  37. D'Agnillo, F., Walters, K.A., Xiao, Y., Sheng, Z.M., Scherler, K., Park, J., Gygli, S., Rosas, L.A., Sadtler, K., Kalish, H., et al. (2021). Lung epithelial and endothelial damage, loss of tissue repair, inhibition of fibrinolysis, and cellular senescence in fatal COVID-19. *Sci.*

- Transl. Med. 13, eabj7790. <https://doi.org/10.1126/scitranslmed.abj7790>.
38. Bedi, S., and Ono, A. (2019). Friend or foe: The role of the cytoskeleton in influenza A virus assembly. *Viruses* 11. <https://doi.org/10.3390/v11010046>.
  39. Mendonça, L., Howe, A., Gilchrist, J.B., Sheng, Y., Sun, D., Knight, M.L., Zanetti-Domingues, L.C., Bateman, B., Krebs, A.S., Chen, L., et al. (2021). Correlative multi-scale cryo-imaging unveils SARS-CoV-2 assembly and egress. *Nat. Commun.* 12, 4629. <https://doi.org/10.1038/s41467-021-24887-y>.
  40. Pepe, A., Pietropaoli, S., Vos, M., Barba-Spaeth, G., and Zurzolo, C. (2022). Tunneling nanotubes provide a route for SARS-CoV-2 spreading. *Sci. Adv.* 8. <https://doi.org/10.1126/sciadv.abo0171>.
  41. Ghosh, S., Dellibovi-Ragheb, T.A., Kerviel, A., Pak, E., Qiu, Q., Fisher, M., Takvorian, P.M., Bleck, C., Hsu, V.W., Fehr, A.R., et al. (2020).  $\beta$ -Coronaviruses Use Lysosomes for Egress Instead of the Biosynthetic Secretory Pathway. *Cell* 183. <https://doi.org/10.1016/j.cell.2020.10.039>.
  42. Eymieux, S., Uzbekov, R., Rouillé, Y., Blanchard, E., Hourieux, C., Dubuisson, J., Belouzard, S., and Roingard, P. (2021). Secretory vesicles are the principal means of sars-cov-2 egress. *Cells* 10. <https://doi.org/10.3390/cells10082047>.
  43. Barreto-Vieira, D.F., da Silva, M.A.N., de Almeida, A.L.T., Rasinhas, A. da C., Monteiro, M.E., Miranda, M.D., Motta, F.C., Siqueira, M.M., Girard-Dias, W., Archanjo, B.S., et al. (2022). SARS-CoV-2: Ultrastructural Characterization of Morphogenesis in an In Vitro System. *Viruses* 14. <https://doi.org/10.3390/v14020201>.
  44. Bracq, L., Xie, M., Benichou, S., and Bouchet, J. (2018). Mechanisms for cell-to-cell transmission of HIV-1. *Front. Immunol.* 9.
  45. Mukai, H., Toshimori, M., Shibata, H., Takanaga, H., Kitagawa, M., Miyahara, M., Shimakawa, M., and Ono, Y. (1997). Interaction of PKN with  $\alpha$ -actinin. *J. Biol. Chem.* 272. <https://doi.org/10.1074/jbc.272.8.4740>.
  46. Fraley, T.S., Pereira, C.B., Tran, T.C., Singleton, C., and Greenwood, J.A. (2005). Phosphoinositide Binding Regulates  $\alpha$ -Actinin Dynamics. *J. Biol. Chem.* 280. <https://doi.org/10.1074/jbc.m500631200>.
  47. Wu, C.T., Lidsky, P.V., Xiao, Y., Cheng, R., Lee, I., T., Nakayama, T., Jiang, S., He, W., Demeter, J., Knight, M., G., et al. (2023). SARS-CoV-2 replication in airway epithelia requires motile cilia and microvillar reprogramming cell. *Cell* 186, 112–130.e20. <https://doi.org/10.1016/j.cell.2022.11.030>.
  48. Sjöblom, B., Salmazo, A., and Djinić-Carugo, K. (2008).  $\alpha$ -Actinin structure and regulation. *Cell. Mol. Life Sci.* 65. <https://doi.org/10.1007/s00018-008-8080-8>.
  49. Yin, W., Li, W., Li, Q., Liu, Y., Liu, J., Ren, M., Ma, Y., Zhang, Z., Zhang, X., Wu, Y., et al. (2020). Real-time imaging of individual virion-triggered cortical actin dynamics for human immunodeficiency virus entry into resting CD4 T cells. *Nanoscale* 12. <https://doi.org/10.1039/c9nr07359k>.
  50. Rubio, K., Singh, I., Dobersch, S., Sarvari, P., Günther, S., Cordero, J., Mehta, A., Wujak, L., Cabrera-Fuentes, H., Chao, C.M., et al. (2019). Inactivation of nuclear histone deacetylases by EP300 disrupts the MiCEE complex in idiopathic pulmonary fibrosis. *Nat. Commun.* 10. <https://doi.org/10.1038/s41467-019-10066-7>.
  51. Singh, I., Contreras, A., Cordero, J., Rubio, K., Dobersch, S., Günther, S., Jeratsch, S., Mehta, A., Krüger, M., Graumann, J., et al. (2018). MiCEE is a ncRNA-protein complex that mediates epigenetic silencing and nucleolar organization. *Nat. Genet.* 50. <https://doi.org/10.1038/s41588-018-0139-3>.
  52. Edgar, R., Domrachev, M., and Lash, A.E. (2002). Gene Expression Omnibus: NCBI gene expression and hybridization array data repository. *Nucleic Acids Res.* 30, 207–210. <https://doi.org/10.1093/nar/30.1.207>.

## STAR★METHODS

### KEY RESOURCES TABLE

REAGENT or RESOURCE	SOURCE	IDENTIFIER
Experimental models: Cell lines		
A549	ECACC	Cat#86012804
Bacterial and virus strains		
BetaCoV/France/IDF0372/2020	National Reference Center for Respiratory Viruses hosted by Institut Pasteur (Paris, France) and headed by Pr. Sylvie van der Werf	provided by Dr. X. Lescure and Pr. Y. Yazdanpanah and supplied through the European Virus Archive goes Global (EVAg) platform, a project that has received funding from the European Union's Horizon 2020 research and innovation program under the grant agreement No 653316
Antibodies		
M Protein (Rabbit)	Abnova (TEBU-BIO)	Cat# PAB31758
N Protein (Rabbit)	Rockland/TEBU-BIO	Cat# 200-401-A50
N protein (Mouse)	Thermo Fisher	Cat# MA1-7403
S Protein (Mouse)	Sino biologicals	Cat# 40592-MM57
Lamp1 (Mouse)	Santa Cruz	Cat# sc-18821
Rab7 (Mouse)	Santa Cruz	Cat# sc-10767
ER-GRP78 (Goat)	Santa Cruz	Cat# sc-1050
PKN (Mouse)	Santa Cruz	Cat# sc-7969
Alpha-Actinins (Rabbit)	Cell Signaling	Cat # 31345
ERGIC-53-AF647 (Mouse)	Santa Cruz	Cat# sc-385158
PKN ms-IgGk BP-FITC (Mouse)	Santa Cruz	Cat# sc-516140
AF568 (Rabbit)	Thermo Fisher	Cat# A10042
AF633 (Mouse)	Thermo Fisher	Cat# A-21050
AF633 (Goat)	Invitrogen	Cat# 84C1-1
Star Orange (Rabbit)	Abberior	Cat# STORANGE-1002-500UG
Chemicals, peptides, and recombinant proteins		
WGA-647	Thermo Fisher	Cat# W32466
AF488-labeled Phalloidin	Thermo Fisher	Cat# A12379
Star Red Phalloidin	STRED-0100-20UG	Cat# STRED-0100-20UG
Remdesivir	Tebu-bio	Cat# T7766
PKN inhibitor K-252a	Santa Cruz	Cat# 200517
Rho/SRF pathway inhibitor	Sigma Aldrich	Cat# 555558
Rac1 inhibitor EHT1864	Sigma Aldrich	Cat# B0560
Software and algorithms		
Origin 19 software	Origin lab	<a href="https://www.originlab.com/origin">https://www.originlab.com/origin</a>
Image J		<a href="https://imagej.nih.gov/ij/">https://imagej.nih.gov/ij/</a>

## RESOURCE AVAILABILITY

### Lead contact

Further information and requests for resources and reagents should be directed to and will be fulfilled by the lead contact, Delphine Muriaux ([delphine.muriaux@irim.cnrs.fr](mailto:delphine.muriaux@irim.cnrs.fr)).

### Materials availability

This study did not generate new unique reagents.

### Data and code availability

This paper does not report original code. The sequencing data of RNA have been deposited in NCBI's Gene Expression Omnibus (PMID 11752295)<sup>52</sup> and is accessible through SRA Sequence Read Archives NCBI with accession number PRJNA781849.

## METHOD DETAILS

### Cell culture and infection

Human pulmonary Alveolar A549-hACE2 cells, referred as lung cells in this study, were obtained from original A549 (ECACC) transduced with a lentiviral vector expressing human ACE2 receptor (manufactured by FlashTherapeutics company, Toulouse, France) and sorted by cytometry for having more than 80% hACE2 on their surface. The sorted A549-hACE2 cells were maintained in RPMI supplemented with 10% heat inactivated fetal bovine serum (FBS), 1% sodium Pyruvate, 0.5% HEPES and antibiotics (penicillin/Streptavidin) and cultivated at 37°C with 5% CO<sub>2</sub>. For virus production, VeroE6 cells were obtained from (ECACC) and maintained in Dulbecco's minimal essential medium (DMEM) supplemented with 10% heat inactivated fetal bovine serum (FBS) at 37°C with 5% CO<sub>2</sub>. For drug treatment, the lung cells were infected with SARS-CoV-2 (MOI 0.01) and treated with drugs (Remdesivir (Tebu-bio, T7766), PKN inhibitor (K-252a, Santa Cruz, 200517), RhoGTPase inhibitor (Rho/SRF pathway inhibitor Sigma, 555558), Rac1 inhibitor (EHT1864, Sigma B0560)) 16h post-infection, and incubated at 37°C with 5%CO<sub>2</sub> for the rest of the experiment (ie, 48hpi) before further investigation.

The strain BetaCoV/France/IDF0372/2020, was supplied by the National Reference Center for Respiratory Viruses hosted by Institut Pasteur (Paris, France) and headed by Pr. Sylvie van der Werf. The human sample from which strain BetaCoV/France/IDF0372/2020 was isolated has been provided by Dr. X. Lescure and Pr. Y. Yazdanpanah from the Bichat Hospital, Paris, France. Moreover, the BetaCoV/France/IDF0372/2020 strain was supplied through the European Virus Archive goes Global (EVAg) platform, a project that has received funding from the European Union's Horizon 2020 research and innovation program under the grant agreement No 653316. COV-2 Virus was propagated in VeroE6 cells with DMEM containing 2.5% FBS at 37°C with 5% CO<sub>2</sub> and harvested 72 hours post inoculation. Virus stocks were stored at -80°C and titer using plaque assays as previously described (11).

### Transfected cells

Human pulmonary A549 cells were transfected with plasmids expressing Wuhan SARS-CoV-2 M, N, E or S proteins (described in Gourdelier et al., 2022) using Lipofectamine3000 (ThermoFisher) transfection reagent as manufacturer protocole, for 48h with a ratio of plasmids of 0,3 µg for each M, N and E plasmids, and 0,5µg for S plasmid. After 48h, transfected cells were washed with PBS, fixed in 4% paraformaldehyde in PBS for 15 minutes at room temperature and proceed for imaging as described in the next section.

### Immuno-fluorescence confocal, Airy Scan and 2D/3D STED super-resolution microscopy

A549-hACE2 cells seeded on glass coverslips were infected with SARS-CoV-2 at a MOI=0.01 (low multiplicity of infection). At different time interval from 6h to 77h post-infection cells were washed with PBS and fixed in 4% paraformaldehyde in PBS for 15 minutes at room temperature, followed by permeabilization with 0.2% Triton X-100 in PBS for 4-5 minutes and blocking in 2% BSA in PBS for 15 min. Incubation with primary antibodies anti-SARS-CoV2 rabbit membrane (M) protein (1:100), mouse anti-N protein (1:25), mouse anti-Spike (1:100), Goat anti-ER-GRP78 (Santa cruz biotechnology, cat# sc-1050, 1:100), rabbit anti alpha-Actinins (Cell signalling, cat#3134s, 1:100), mouse anti-Lamp1 (Santa cruz biotechnology, cat# sc-18821, 1:100) and mouse anti-Rab7 (Santa cruz biotechnology, cat#sc-376362, 1:100), mouse anti-PKN (Santa Cruz biotechnology, cat#sc-7969, 1:100), ERGIC-53-AF647 (Santa Cruz biotechnology, cat#sc-385158, 1:100), were performed for 2 hours at room temperature. After washing with PBS, cells were incubated with secondary antibodies AF633- labeled anti-mouse, goat (1:250), AF568-labeled goat-anti-rabbit (1:250), for PKN ms-IgGk BP-FITC (2ndary antibody) and Star orange for high resolution STED imaging (1:100) as well as AF488-labeled Phalloidin and Star Red phalloidin (1:100) (for STED microscopy) for 2 hours at room temperature. We have used Wheat germ agglutinin-AF647-conjugate (Thermofisher

scientific) for membrane labelling (10 min incubation time at room temperature). We have used mounting media prolong gold antifade reagent with DAPI and prolong gold antifade reagent without DAPI for confocal and STED microscopy respectively. Confocal fluorescence images were generated using a LSM780 confocal laser-scanning microscope (Zeiss) equipped with a 63X, 1.4 NA oil objective, Airy scan fluorescence images were generated using a LSM980-laser-scanning microscope (Zeiss) equipped with a 63X, 1.4 NA oil objective and STED 2D and 3D measurements were performed on the Abberior Instrument Expert Line STED super-resolution microscope (Abberior Instruments GmbH, Göttingen, Germany) using Star orange 580 and Star red pulsed excitation laser sources with a pulsed STED laser operating at 775 nm. For STED 2D (25% laser) lateral resolution was 67nm and for STED 3D (30% laser) resolution was 185 nm in Z. We have done 3 times independent experiments for each study. All the images were processed with ImageJ/Fiji software. For 3D-reconstruction of STED images Imaris viewer was used.

### Quantitative reverse transcription polymerase chain reaction (qRT-PCR)

RNAs from mock infected or infected (MOI=0.01) A549-hACE2 cell culture supernatant were extracted using the Nucleospin Dx Virus RNA purification kit (Macherey-Nagel). Then qRT-PCR was performed in triplicate as described<sup>20</sup>, using primers targeting the E gene of SARS-CoV-2 (E\_Sarbeco-Forward ACA GGTACGTTAATAGTTAATAGCGT; E\_Sarbeco-Reverse ATATTGCAGCAGTACGCACACA) and Luna Universal One-Step qRT-PCR Kit (New England Biolabs) on a Roche Light Cycler 480. The calibration of the assay was performed with a nCoV-E-Sarbeco-Control Plasmid (Eurofins Genomics).

### RNA sequencing and data analysis

RNA was sequenced as previously described by Fraley et al.,<sup>46</sup> and Wu et al.<sup>47</sup> Briefly, total RNA from non-infected (Ctrl) or SARS-CoV-2 infected A549-hACE2 and hPCLS was isolated using Trizol (Invitrogen). RNA was treated with DNase (DNase-Free DNase Set, Qiagen) and repurified using the miRNeasy micro plus Kit (Qiagen). Total RNA and library integrity were verified on LabChip Gx Touch 24 (Perkin Elmer). One  $\mu$ g of total RNA was used as input for SMARTer Stranded Total RNA Sample Prep Kit-HI Mammalian (Clontech). Sequencing was performed on the NextSeq500 instrument (Illumina) using v2 chemistry with 1x75bp single end setup. Raw reads were visualized by FastQC to determine the quality of the sequencing. Trimming was performed using trimmomatic with the following parameters LEADING:3 TRAILING:3 SLIDING-WINDOW:4:15 HEADCROP:4, MINLEN:4. High quality reads were mapped using with HISAT2 v2.1.0 with reads corresponding to the transcript with default parameters. RNA-seq reads were mapped to human genome hg19. After mapping, Tag libraries were obtained with MakeTaglibrary from HOMER (default setting). Samples were quantified by using analyzeRepeats.pl with the parameters (hg19 -count genes -rpk; reads per kilobase per millions mapped).

### RNA-seq based expression analysis of viral transcripts

Fastq files from infected A549-hACE2 cells after 24h, and 48h were used as input; for each timepoint we used 2 replicates. Read trimming was performed using trimmomatic (v 0.39) with the following parameters "ILLUMINACLIP:all\_adapters\_v0.38.fa:2:30:10 AVGQUAL:30 LEADING:0 TRAILING:0 SLIDINGWINDOW:6:30 MINLEN:38". Trimmed reads were then aligned to the SARS-CoV-2 reference genome NC\_045512.2.fasta (downloaded May 2021 from [https://www.ncbi.nlm.nih.gov/nucleotide/NC\\_045512](https://www.ncbi.nlm.nih.gov/nucleotide/NC_045512)) using the STAR (v 2.7.9a) aligner; STAR parameters were the following "-outFilterType BySJout -outFilterMultimapNmax 20 -alignSJoverhangMin 8 -outSJfilterOverhangMin 12 12 12 12 -outSJfilterCountUniqueMin 1 1 1 1 -outSJfilterCountTotalMin 1 1 1 1 -outSJfilterDistToOtherSJmin 0 0 0 0 -outFilterMismatchNmax 999 -outFilterMismatchNoverReadLmax 0.04 -scoreGapNoncan -4 -scoreGapATAC -4 -chimOutType WithinBAM HardClip -chimScoreJunctionNonGTAG 0 -alignIntronMin 20 -alignIntronMax 1000000 -alignMatesGapMax 1000000 -alignSJstitchMismatchNmax -1 -1 -1 -1". Samtools (v 1.12) was used to handle the alignments, and bedtools coverage was used to count reads in each viral feature (gene) using the genomic coordinates from GCF\_009858895.2\_ASM985889v3\_genomic.gff (downloaded May 2021 from [https://ftp.ncbi.nlm.nih.gov/genomes/all/GCF/009/858/895/GCF\\_00985889v3/GCF\\_00985889v3/GCF\\_00985889v3\\_ASM985889v3\\_genomic.gff.gz](https://ftp.ncbi.nlm.nih.gov/genomes/all/GCF/009/858/895/GCF_00985889v3/GCF_00985889v3/GCF_00985889v3_ASM985889v3_genomic.gff.gz)) only for protein coding features.<sup>46,47</sup> Feature counts were transformed to reads per kilobase million (RPKM) we calculated mean RPKM from the duplicates for each feature and then calculated a Fold Change as mean RPKM at 48h / mean RPKM at 24h; this data handling and plotting was performed using R.

### Western Blot analysis

A549-hACE2 cells were infected for 2 hours with SARS-CoV-2 (MOI = 0.01). At different time point (6h, 24h, 48h, 54h, 72h and 77h) post infection (pi), cells were washed twice in PBS, detached with Versen (0.1M EDTA), pelleted at 250g for 6min and lysed in RIPA buffer for western blot analysis. Total protein concentration was calculated using a Bradford protein assay kit (ThermoFisher). 20µg of total cell lysates were diluted in Laemmli buffer and proteins were separated by SDS-PAGE on 8% (for CoV-2 S- and N proteins) and 12% (for CoV-2 M protein) acrylamide gels. Gels were transferred to PVDF membrane using wet transfer with Tris-glycine-methanol buffer. Membranes were washed in TBS, blocked with 5% milk in TBS-Tween 0.1% for 30min and incubated overnight at 4°C with primary antibodies against the spike S protein (Gentex, cat# GTX632604), N-protein (Gentex, cat# GTX632269) or M-protein (Tebu, cat# 039100-401-A55), all three diluted at 1:1000 in TBS-T. After washing with 5% milk in TBS-Tween, the membranes were incubated with HRP conjugated anti-mouse antibodies for N and S protein, and with HRP conjugated anti-rabbit antibody for M protein and alpha-actinins for 2h at room temperature, then washed in TBS-Tween buffer, incubated with ECL reagent (Amersham cat#RPN2236) and imaged using a Chemidoc Imager (Biorad).

### Electron microcopy

A549-hACE2 pulmonary cells infected with SARS-CoV-2 were fixed with 2,5% (v/v) glutaraldehyde in PHEM buffer and post fixed in osmium tetroxide 1% /  $K_4Fe(CN)_6$  0,8%, at room temperature for 1h for each treatment. The samples were then dehydrated in successive ethanol bathes (50/70/90/100%) and infiltrated with propylene oxide/ EMBED812 mixes before embedding. 70 nm ultrathin cuts were made on a PTXL ultramicrotome (RMC, France), stained with OTE/lead citrate and observed on a Tecnai G2 F20 (200kV, FEG) TEM at the Electron Microscopy Facility COMET, INM, Platform Montpellier RIO Imaging, Biocampus, Montpellier.

## QUANTIFICATION AND STATISTICAL ANALYSIS

### Image analysis

For confocal images, the viral M clusters area for different conditions were measured using segmentation (ImageJ/Fiji). A schematic representation for details of the segmentation methods is given in [Figure S1](#). Viral particles size from STED images were also analysed using segmentation (ImageJ). The mean fluorescence intensity of F-actin, alpha-Actinins and ER-GRP78 labelling were measured using ImageJ. For Mean intensity analysis, images were acquired using a confocal microscope. To ensure reasonable quantification among conditions, all images were taken with the same objective and microscope settings. For post-processing, individual cells, which are well separated from each other were chosen. Z-stacks with 0.3 micrometer slices per cell were chosen to ensure the whole cell slicing in focus. The resulting Z-projection images of individual cells were used to calculate the mean fluorescence intensity of each cell for each labelling. In addition, we calculated the cell area, volume and height using 3D viewer plugin from ImageJ. From STED and Airy scan images the diameter sizes of F-actin, Rab7, Lamp1 and viral rings were determined “manually” for each ring using ImageJ software. Mander’s colocalization analysis done by using JACoP plugin of Image J software.

### Angle of orientation analysis

From STED 2D microscopy images of F-actin, the orientations of the nano-fibers angles were evaluated based on the structure tensor of each nano-fibers compares to its local neighborhood using the Java plugin for ImageJ “OrientationJ”. From the given images, the OrientationJ plugin computes the structure tensor for each pixel in the image by sliding the Gaussian analysis window over the entire image. The local angle of orientation properties encoded in color and it is also generating a distribution of angles for each nano-fibers for a given image. Here, in the STED images, it is considered the vertically elongated nano-fibers as the major orientation angle (as around +90 Deg and – 90 Deg from the cell edge) and others orientation angles were calculated accordingly. Area are normalized to the distribution curve of angles to compare the changes in distribution for infected and non-infected cell (as in [Figure 3B](#)).

### Statistical analysis

Statistical tests were performed using Origin 2021 software. One-way analysis of variance (ANOVA) and Mann-Whitney test was used for group comparisons. ns,  $P > 0.05$ , \* $P \leq 0.05$ , \*\* $P \leq 0.01$ , \*\*\* $P \leq 0.001$ , and \*\*\*\* $P \leq 0.0001$ .